Homogeneous Hydrogen Evolution Catalyst Assessment and Design towards the Development of a Photocatalytic Molecular Device

Aaron J. Goodman, Emily G. Nelson, Bart M. Bartlett*

A Thesis Submitted in Partial Fulfillment of the

Requirements for the Degree of Bachelor of Science

With Honors in Chemistry from the

University of Michigan

2012

University of Michigan, Department of Chemistry

930 N. University Avenue

Ann Arbor, MI 48109

Abstract

The complex $[(bpy)_2MoO]^{2+}$ was synthesized. The complex was evaluated as an electrocatalyst for proton reduction from *p*-toluenesulfonic acid in DMSO. The catalyst was found to release hydrogen with a rate constant k_{cat} = 1.24 Hz at -1.85 V vs. $Fc^{+/0}$, and to evolve hydrogen with 95% faradaic efficiency. The rate of hydrogen evolution was first-order in catalyst and second-order in acid.

The complex $[(bdt)_2MoO]^{2-}$ was synthesized. The complex was evaluated as an electrocatalyst for proton reduction from acetic acid in acetonitrile. The rate of hydrogen evolution was first-order in catalyst and second-order in acid. The catalytic mechanism has been proposed to proceed via the following steps: 1) The catalyst was once reduced at a potential of -0.87 V vs. $Fc^{+/0}$. This reduction was primarily metal based. 2) The catalyst was reduced at -1.89 V vs. $Fc^{+/0}$, and simultaneously twice protonated at the nucleophilic oxygen and a basic sulfur. 3) The complex then eliminated H_2 regenerating $[(bdt)_2MoO]^{2-}$.

The complex $[Ru(bpym)(bpy)_2]^{2+}$ was evaluated as a light sensitizer for use in a photocatalytic molecular device. The ^{3}MLCT emissive state in $[Ru(bpym)(bpy)_2]^{2+}$ was found to have sufficient energy to photo reduce the catalytic motif $[(bpym)_2MoO]^{2+}$ in the proposed molecular photocatalyst, $[(bpy)_2Ru(bpym)Mo^{IV}O(bpym)Ru(bpy)_2]^{6+}$.

Table of Contents

Chapter 1: Introduction

Motivation –

The annual average rate of global energy consumption is predicted to at least double by 2050 to approximately 28-35 terawatts.[1] Most of the energy consumed today comes from fossil fuels such as coal and oil. The demand for energy endangers the economy, environment, and global political health. For instance, current atmospheric carbon dioxide levels of 380 ppm are higher than they have been for the last 650,000 years.[2] In order to protect the environment, make energy more universally accessible, and quell political conflicts, some of the fossil fuels in use today must be replaced with sustainable sources.

The photoelectrolysis of water using solar energy servers as a possible source of renewable energy. The two half reactions of the electrolysis of water are represented in the equations below:

$$4H^+ + 4e^- \rightarrow 2H_2 \qquad E_{cathode} = [0 - 0.059(pH)]\,V\ vs.NHE$$
$$2H_2O \rightarrow O_2 + 4H^+ + 4e^- \qquad E_{anode} = [1.23 - 0.059(pH)]\,V\ vs.NHE$$
$$2H_2O \rightarrow O_2 + 2H_2 \qquad E_{reaction} = E_{anode} - E_{cathode} = -1.23\,V$$

The 1.23 V per electron corresponds to a change in Gibbs free energy, $\Delta_{rxn}G^0$=237.2 kJ•mol^{-1}.[3] The voltage required for the reaction to proceed corresponds to an average of 1.23 eV per electron. Depending on the mechanism through which each half reaction proceeds, some of the electrons will require a much greater potential than what is predicted by the change in free energy of the reaction. This extra energy required is

---

[1] Lewis, N.S.; Nocera, D.G. *Proc. Nat. Acad. Sci. U.S.A.* **2006**, *103*, 15729.
[2] Siegenthaler, U.; Stocker, T.F.; Monnin, E.; Luthi, D.; Schwander, J.; Stauffer, B.; Raynaud, D.; Barnola, J.-M.; Fischer, H.; Masson-Delmotte, V.; Jouzel, J. *Science* **2005**, *310*, 1313.
[3] $\Delta_{rxn}G^0 = -nFE^0_{rxn}$

visible, for example, in the large overpotential required to oxidize water in the absence of a catalyst.

Photocatalytic Water Splitting, a Historical Perspective –

The first photoelectrochemical experiment was performed in 1839 by Becquerel, who observed a photovoltage when he illuminated a silver chloride electrode connected to a counter electrode in solution.[4,5] This "Becquerel Effect" was first exploited for the conversion of solar energy to fuel in the context of the photoelectrolysis of water in the ground-breaking experiments of Fujishima and Honda who connected a TiO_2 electrode to a platinum electrode and observed current when the TiO_2 electrode was illuminated with ultraviolet light.[6]

Hydrogen as Fuel –

People have since been fascinated by the prospect of directly splitting innocuous water into hydrogen fuel and oxygen using sunlight, and for good reason; there are many advantages to using sunlight to photoelectrolyze water. The conversion of sunlight into fuel as opposed to electricity or heat is advantageous, because fuel is more easily stored.

In particular, hydrogen gas has much potential as environmentally benign fuel. The combustion of H_2 generates only water. If the photoelectrolysis of water is the source of the fuel, the entire cycle is completely carbon (and CO_2) neutral. Furthermore, hydrogen is very flexible as a fuel; [7,8] its use not limited to traditional combustion. Most

---

[4] Nozik, A.J. *Ann. Rev. Phys. Chem.* **1978**, *29*, 189-222.
[5] Becquerel, E. *C. R. Acad. Sci.* **1839**, *9*, 561.
[6] Fujishima, A.; Honda, K. *Nature* **1972**, *238*, 37.
[7] Winsche, W.E.; Hoffman, K.C.; Salzano, F.J. *Science*, **1973**, *180*
[8] Gregory, D.P. *Sci. Am.* **1973**, *228*, 13.

notably, it can be used in fuel cells to generate electricity with high efficiency.[9] In addition, many chemical reductions, petroleum refining, and nitrogen fixation (N_2 +3H_2 → 2NH_3) via the energy intensive Haber process require H_2 as a reactant.

There are many possible routes to H_2 fuel, and several are mapped out in *Figure 1* below.[10] An important alternative to the direct photoelectrolysis of water is the electrolysis of water powered by a photovoltaic (PV) cell. At this point in time, neither the direct photoelectrolysis of water, nor PV/electrolysis is sufficiently robust, scalable, and efficient to meet global energy needs.[11] Photovoltaics and photoelectrolysis are both heavily researched today, and both have potential to develop into viable, global-scale renewable energy sources. This paper will examine catalysis and photochemistry relevant to the direct photoelectrolysis of water. The direct photoelectrolysis of water is so attractive, that in 1995, Bard and Fox introduced the term, "Holy Grail", to describe a robust, scalable, and efficient system to produce H_2 to compete with fossil fuels.[12] There is still much work to be done to achieve this goal.

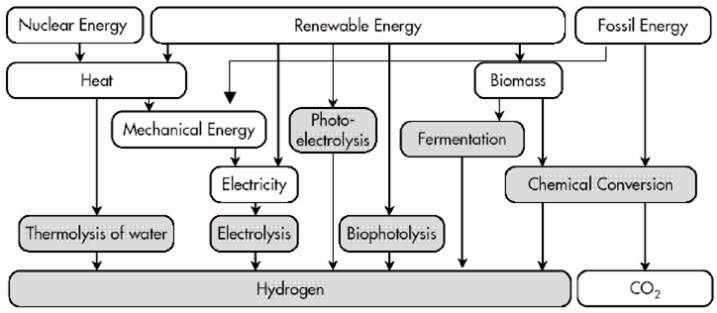

Figure 1. There are several routes to hydrogen. Two popular routes from solar are electrolysis power by a photovoltaic device and the direct photoelectrolysis of water.

[9] Kralj, A.K.; Glavic, P. *Energy & Fuels* **2007**, *21*, 2892-2899.
[10] Turner, J.A. *Science*, **1999**, *285*, 687-689.
[11] Yang, P. (2012, March) *Nanowire Building Blocks: From Flux Line Pinning to Artificial Photosynthesis*. Speech presented at UofM, Ann Arbor, MI.
[12] Bard, A.J.; Fox, M.A. *Acc. Chem. Res.* **1995**, *28*, 141-145.

Energetics of Water Splitting –

Fujishima and Honda split water using one photoelectrode (TiO_2). The band edges of TiO_2 are properly positioned to split water. *Figure 2* below illustrates the band-edge requirements for splitting water with one photoelectrode. When an incident photon with energy greater than the band gap is absorbed by the material, an electron is promoted from the conduction band to the valence band, leaving behind an oxidizing hole in the valence band. The excited electron goes to reduce protons, and the hole accepts electrons from water.

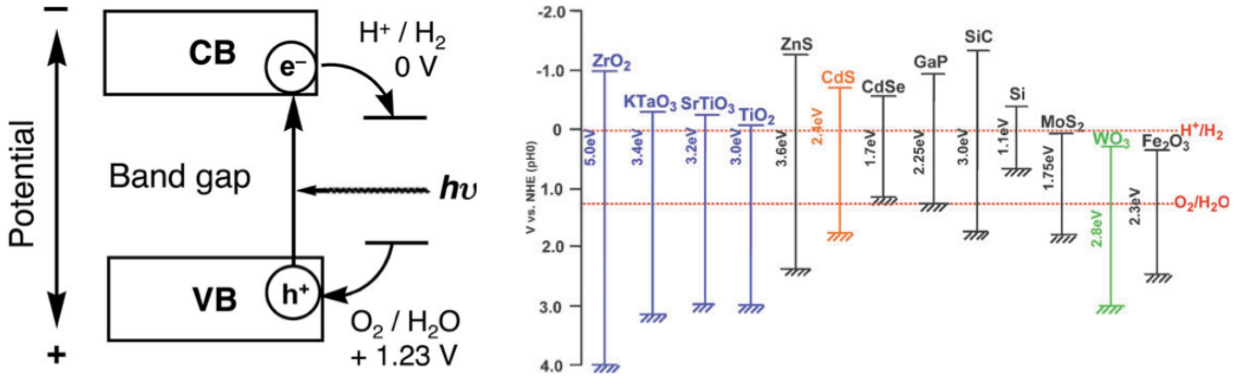

Figure 2. In order for a single material to photocatalytically split water, it's valence band (VB) (HOMO in a molecular system) must be lower in energy than the O_2/H_2O reduction potential, and it's conduction band (CB) (molecular orbital occupied upon excitation in a molecular system), must be higher in energy than the H^+/H_2 reduction potential (left). There are many materials (right) whose CB and VB straddle the half reaction potentials.

For these events to happen in sunlight, the band gap ($E_{VB} - E_{CB}$) and the absolute position of the band edges are critical.[13] The top of the valence band must be more positive than the O_2/H_2O redox potential, and the bottom of the conduction band must be more negative than the H^+/H_2 redox potential. These thermodynamic requirements imply a minimum band gap of 1.23 eV, which corresponds to photons with wavelengths of 1100 nm (near IR). On the other hand, the band gap must be

[13] Kudo, A.; Miseki, Y. *Chem. Soc. Rev.* **2009**, *38*, 253.

sufficiently small to absorb a significant portion of the solar spectrum (the orange curve in *Figure 3* represents the solar irradiance as a function of wavelength at the Earth's surface), which outputs little light with wavelength less than 400 nm (3.1 eV). Finding a material to act as a photoelectrode in single-absorber system like Fujishima and Honda's is difficult, because the band edge requirements are very specific. When one realizes that both band edges must also incorporate a significant overpotential, the problem becomes even more difficult.

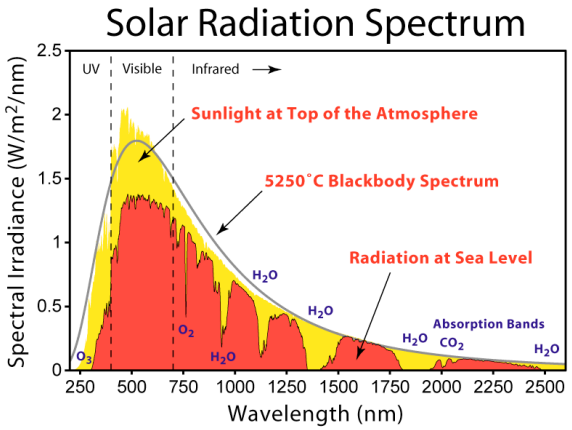

Figure 3. The sun outputs radiation with the approximate profile of a 5250°C blackbody (black line). Much of that radiation is absorbed by the atmosphere leaving the radiation spectrum represented by the red line (AM 1.5). In order for a solar powered device to efficiently capture the suns energy, it must absorb efficiently in visible or IR light

The Advantages of Using Two Light Absorbers: Z-Scheme Chemistry –

It is possible to perform each half reaction at two spatially separated light absorbers. Electrons that are extracted from water at the oxidation half reaction are transferred to reduce protons at the reduction half reaction via a conducting medium. The ions produced by each half reaction diffuse between the reactions, completing the circuit. In photosynthesis, this reaction scheme is termed Z-scheme chemistry (see *Figure 4* below), and has several marked advantages.

Because the reactions are spatially separated, there is no need to separate the products, (H_2 and O_2 in the photoelectrolysis of water) before use. The band edge energy (HOMO/LUMO energies in a molecular system) requirements for each material

are relaxed, because, each material only need to perform one reaction. In addition, each material can drive its reaction with higher energy holes or electrons, while still absorbing much of the solar spectrum. For example, $CuWO_4$-WO_3 is a photoanode with good light absorption properties capable of oxidizing water. Its conduction band however, is too positive for the material to reduce protons.[14] Employing an additional light absorber in the reduction half-reaction (Z-scheme chemistry) would enable one to take advantage of $CuWO_4$-WO_3's favorable properties as a photoanode (see *Figure 4*).

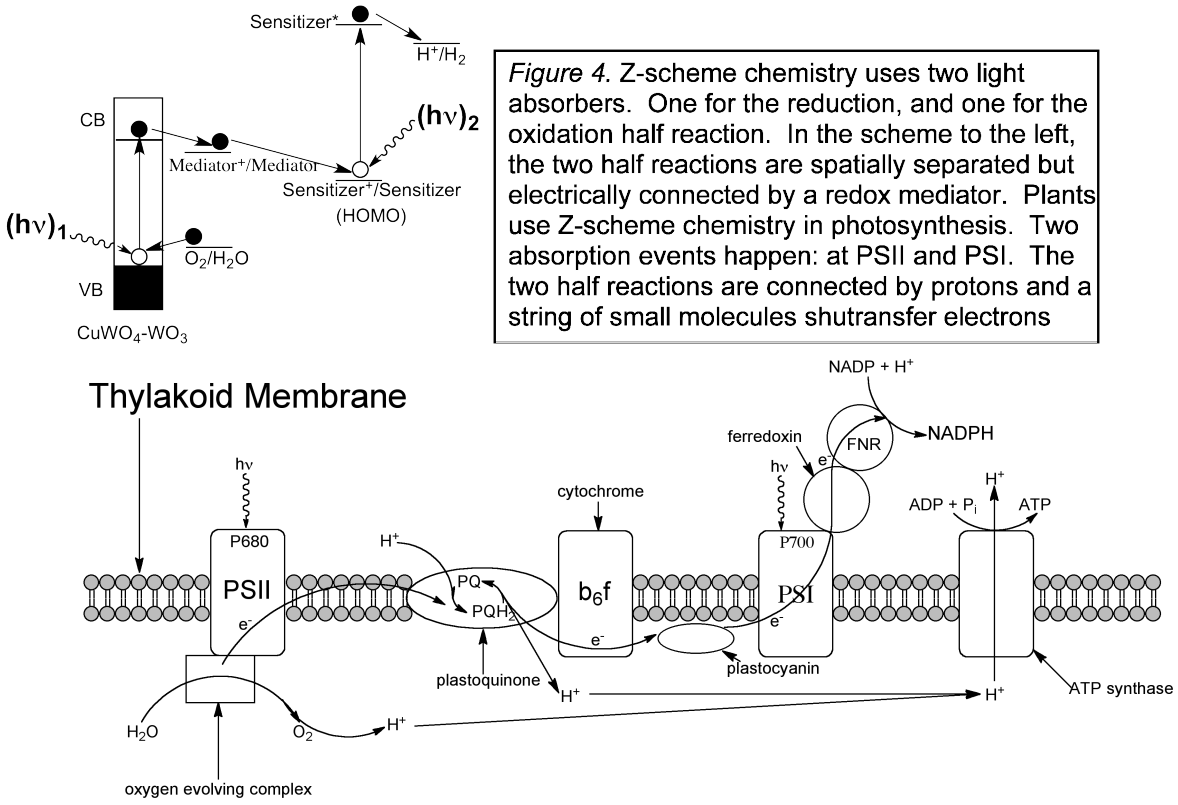

Figure 4. Z-scheme chemistry uses two light absorbers. One for the reduction, and one for the oxidation half reaction. In the scheme to the left, the two half reactions are spatially separated but electrically connected by a redox mediator. Plants use Z-scheme chemistry in photosynthesis. Two absorption events happen: at PSII and PSI. The two half reactions are connected by protons and a string of small molecules shutransfer electrons

Using two materials, each requiring less than 1.23 eV of energy allows for more efficient collection of the solar spectrum. If the necessary 1.23 eV is collected via two separate absorption events, each material can absorb lower energy photons. Quantitatively, single-band gap devices have a solar conversion efficiency limit of 32%,

[14] Yourey, J.E.; Kurtz, J.B.; Bartlett, B.M. *J. Phys. Chem. C* **2012**, *116*, 3200.

while dual-band gap devices have an efficiency limit of 42%.[15] There are many examples in the literature that have attempted to utilize the advantages of dual-band gap devices, from two simultaneously illuminated semiconductor systems,[16,17,18] to monolithic layered electrodes. A notable of example of which has achieved one of the highest solar energy to fuel conversion efficiencies to date, 12.4%.[19] The top layer of this cell is a *p*/*n* $GaInP_2$ junction (E_g=1.83 eV), which absorbs the visible portion of the spectrum, while transmitting the IR portion of the spectrum to be absorbed by a *p*/*n* GaAs junction (E_g=1.42 eV). The layers are separated by an integrated diode layer to adjust the two outer layers' band positions to accomplish both water splitting half reactions.

A Z-scheme system requires materials capable of photo-oxidation and photo-reduction. The properties required of each material would be relaxed if each were aided by a catalyst to lower the overpotential necessary for the half-reaction to proceed.

Water Splitting Catalysis –

When discussing the energetics of water splitting, it was glossed over that in reality, both water oxidation and proton reduction require more energetic holes and electrons respectively than is dictated by the reactions' thermodynamics. The anodic and cathodic overpotentials required make band engineering, and material design even more challenging.

---

[15] Bolton, J.R.; Strickler, S.J.; Connolly, J.S. *Nature* **1985**, *316*, 495.
[16] Yoneyama, H.; Sakamoto, H.; Tumura, H. *Electrochem. Acta* **1975**, *20*, 341.
[17] Nozik, A.J. *Appl. Phys. Lett.* **1989**, *29*, 150.
[18] Kainthla, R.C.; Zelenay, B.; Bockris, O. *J. Electrochem. Soc.* **1987**, *134*, 841.
[19] Khaselev, O.; Turner, J.A. *Science*, **1998**, *280*, 425.

Water oxidation is a four-electron reaction, and is kinetically very challenging. The mechanism for water oxidation has been heavily investigated at the surface of many materials including metal oxides,[20] perovskites,[21] and precious metals such as platinum.[22] In general, the reaction undergoes steps analogous to those represented in the scheme below. There are four single electron oxidations, with the most energetically and kinetically demanding resulting in the generation of a physisorbed peroxide intermediate (*step b*).

$$\begin{aligned}
&\textit{step a}: && M^z + OH^- && \leftrightarrow && M^z\text{–}OH + e_1^- \\
&\textit{step b}: && M^z\text{–}OH + OH^- && \xrightarrow{rds} && M^z\cdots H_2O_2 + e_2^- \\
&\textit{step c}: && (H_2O_2)_{phys} + OH^- && \leftrightarrow && (HO_2^-)_{phys} + H_2O \\
&\textit{step d}: && (H_2O_2)_{phys} + (HO_2^-)_{phys} && \leftrightarrow && H_2O(e_3^-) + OH^-(e_4^-) + O_2\uparrow
\end{aligned}$$

While there are many examples of molecular[23] and solid-state[24] water oxidation catalysts in the literature, it is understandably a popular area in research today, with a focus on generating Earth-abundant catalysts with minimal overpotential.

Proton reduction is most readily catalyzed at platinum group metals,[25] at which the mechanism is well understood.[26] The mechanism is illustrated in the scheme below. Atomic hydrogen is chemisorbed to catalytic noble metals (Pt, Rh, Ir, Pd, Ru)[27] at

---

[20] Matsumoto, Y.; Sato, E. *Mater. Chem. Phys.* **1986**, *14*, 397.
[21] Bockris, J.O.; Otagawa, T. *J. Phys. Chem.* **1983**, *87*, 2960.
[22] Conway, B.E.; Liu, T. *Langmuir* **1990**, *6*, 268.
[23] a) Meyer, T.J. *Inorg. Chem.* **2008**, *47*, 1727. b) Schley, N.D.; Blakemore, J.D.; Subbaiyan, N.K.; Incarvito, C.D.; D'Souza, F.; Crabtree, R.H.; Brudvig, G.W. *J. Am. Chem. Soc.* **2011**, *133*, 10473-10481. c) Kanady, J.S.; Tsui, E.Y.; Day, M.W.; Agapie, T. *Science* **2011**, *333*, 733.
[24] Esswein, A.J.; Surendranath, Y.; Reece, S.Y.; Nocera, D.G. *Energy Environ. Sci.* **2011**, *4*, 499.
[25] Trasatti, R.S. *J. Electroanal. Chem.* **1972**, *39*, 163.
[26] Conway, B.E.; Tilak, B.V. *Electrochim. Acta.* **2002**, *47*, 3571.
[27] Tafel, J. *Zeit fur Phys. Chem.* **1905**, *50*, 641.

potentials positive of the H^+/H_2 reduction potential. Hydrogen evolution then occurs at a finite overpotential proceeding from the chemisorbed atomic hydrogen intermediate.

$$H_3O^+ + e^- + M \rightarrow MH_{ads} + H_2O \quad Step\ I$$
$$MH_{ads} + H_3O^+ + e^- \rightarrow H_2\uparrow + H_2O \quad Step\ II$$
$$2MH_{ads} \rightarrow 2M + H_2\uparrow \quad Step\ III$$

In the scheme above, Step I is either followed by step II or II[28] depending on the surface coverage of chemisorbed hydrogen. The favorable catalytic properties of the noble metals are a result of their ability to stabilize chemisorbed H•.

In nature, proton reduction occurs at homogenous Fe-Fe and Ni-Fe sites within hydrogenase enzymes. These natural catalysts utilize Earth-abundant metals to catalyze thousands of turnovers per second at overpotentials less than 100 mV.[29,30] Homogenous catalysts that wish to mimic nature's success must effectively drive catalysis along a two-electron redox pathway to overcome the 1.8 V barrier associated with single-electron proton reductions.[31]

One recent example in the literature to accomplish this is a high valence oxomolybdenum center supported in a pentadendate ligand, 2,6-bis(1,1-bis(2-pyridyl)ethyl)pyridine (PY5Me2).[32] Shown in *Figure 5* below, the catalyst possesses flexible redox chemistry with four formal oxidation states within a 1 V potential window in water. Controlled potential coulometry experiments have indicated that the catalyst has a turnover number greater than 10^5.

---

[28] Conway, B.E.; Tilak, B.V. in: Eley, D.D.; Pines, H., Weisz, P.B. (Eds.), Chapter 1 in Advance in Catalysis, vol. 38, Academic Press Inc., New York, 1992.
[29] Yang, J.R.; Bullock, R.M.; Dubois, M.R.; Dubois, D.L. *MRS Bulletin* **2011**, *36*, 39.
[30] Armstrong, F.A.; *Curr. Opin. Chem. Biol.* **2004**, *8*, 133.
[31] Esswein, A.J.; Nocera, D.G. *Chem. Rev.* **2007**, *107*, 4022.
[32] Karunadasa H.I.; Chang, C.J.; Long, J.R. *Nature* **2010**, *464*, 1329.

The Chang and Long groups have done much work to optimize this catalyst, illustrating many of the advantages of working with homogeneous catalysts, taking advantage of their ability to synthetically alter the catalyst's characteristics. Notably, they have substituted the ligand framework with electron withdrawing groups to markedly decrease the overpotential required to evolve hydrogen at the catalyst (a decrease of 260 mV).[33]

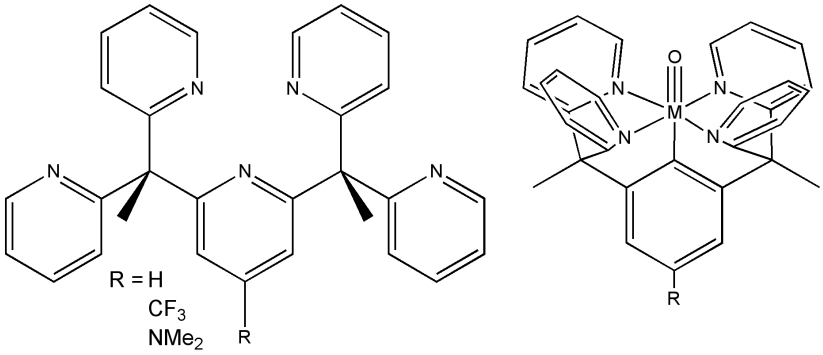

Figure 5. The pentadendate ligand developed in the Long group at Berkeley supports a high-valence oxomolybdenum catalytic site in water. The homogeneous catalyst was synthetically altered by subsituting strongly electron-withdrawing and electron donating groups at the position labeled 'R'. These substitutions greatly affected the overpotential; the electron-withdrawing CF_3 derivative had an overpotential 250 mV smaller than the unsubstituted version.

In addition to synthetic flexibility, molecular catalysts can be effectively modeled computationally, because the active site is better defined than in a heterogeneous catalysts.[34] For example, computational studies of the oxomolybdenum catalyst motif[35] indicate that proton reduction proceeds via reductive cleavage of H_2O followed by α-H abstraction. Computational techniques complement experimental study of the catalytic

[33] Sun, Y.; Bigi, J.P.; Piro, N.A.; Tang, M.L.; Long, J.R.; Chang, C.J. *J. Am. Chem. Soc.* **2011**, *133*, 9212.
[34] Zambeli, T.; Wintterlin, J.; Trost, J.; Ertl, G. *Science* **1996**, *273*, 1688.
[35] Li, J.; Yoshizawa, K. *Angew. Chem. Int. Ed.* **2011**, *50*, 11972.

cycle by spectroscopic techniques (IR, NMR,UV-vis) available to molecular systems in solution.

In light of the above complex's ability to evolve hydrogen, molybdenum's relative abundance, and the ease of mechanistic study and catalyst design in homogenous systems, a homogeneous oxomolybdenum catalyst was designed with the intention of integrating the catalytic motif into a photocatalytic system for proton reduction.

Chapter 2: Experimental

Materials and General Considerations –

Synthetic reagents were used as received. All solvents were reagent grade or higher purity, and were dried and distilled using standard methods under nitrogen. Tetrabutylammonium hexafluorophosphate was recrystallized from 200 proof ethanol. Tetrabutylammonium chloride was recrystallized from acetone and diethyl ether. The starting material bis(acetylacetonate) dioxomolybdenum(VI), $[MoO_2(acac)_2]$ was prepared from ammonium molybdate tetrahydrate and acetyl acetone following the published procedure.[36] Ruthenium polypyridyl complexes of the form $[Ru(L\text{-}L)(bpy)_2]^{2+}$ were prepared from bis(bipyridine) ruthenium(II) dichloride dihydrate[37] and the relevant bidendate ligand, L-L, using the published literature procedure.[38] 2,2'-di(trifluoromethyl)-4,4'-bipyridine was prepared from 2-chloro-4-trifluoromethyl-pyridine, catalyzed by *bis*(triphenylphosphine) Nickel(II) dibromide and activated zinc according to the

[36] G. J.-J. Chen, J. W. McDonald, and W. E. Newton, *Inorg. Chem.,* 1976, **15**, 2612-2615.
[37] Sullivan, B.P.; Salmon, D.J.; Meyer, T.J. *Inorganic Chemistry* **1978**, *17*, 3334.
[38] McFarland, S.A.; Lee, F.S.; Cheng, K.A.; Cozens, F.L., Schepp, N.P. *J Am Chem Soc* **2005**, *127*, 7065-7070 (Supporting Information).

published literature procedure.[37] 2,2'-$(COOH)_2$-4,4'-bipyridine and 2,2'-$(COOEt)_2$-4,4'-bipyridine were synthesized from 2,2'-dimethyl-4,4'-bipyridine according to the published literature procedure.[39]

Instrumentation –

Infrared spectra were measured on a Perkin-Elmer spectrum BX. NMR spectra were recorded on a Varian MR400 400 MHz spectrometer. UV-vis spectra were taken on a Varian Cary 5000 UV-Vis-NIR spectrophotometer. Fluorescence spectra were taken on a Horiba Scientific Fluoromax-2 fluorimeter. Hydrogen detection was performed with a Micromass LCT TOF Mass Spectrometer with Electrospray Ionization. The EPR spectra were taken on a Bruker ESR spectrometer.

Electrochemistry –

Both cyclic voltammetry and controlled potential coulometry were performed using a CH Instruments Electrochemical Workstation 660. Cyclic voltammetry was carried out in a typical 3-electrode set–up employing a glassy carbon working electrode, a Pt mesh auxiliary electrode, and a saturated calomel reference electrode (SCE) unless otherwise noted. Ferrocene was added as an internal reference and all potentials are reported against the $Fc^{+/0}$ for comparison, noting that $Fc^{+/0}$ = +0.38 V SCE. 100 mM Bu_4NPF_6 is the electrolyte in all experiments, and all sweeps are performed at a scan rate of 50 mV/s unless otherwise noted.

[39] Case, F.H. *J. Am. Chem. Soc.* **1946**, *68*, 2574.

Syntheses –

bis(2,2'-bipyridine) dioxomolybdenum(VI) $[MoO_2(bpy)_2][OH]_2$ (1) – The complex was prepared by a modification of literature methods.[40] Bipyridine (3.12 g, 20 mmol) was dissolved in ethanol. $MoO_2(acac)_2$ (3.26 g, 9.99 mmol) was then added. The solution was refluxed for 3 h and the precipitate filtered in air, washed with water and dried in vacuo yielding 2.1 g (47%) of white powder.

bis(2,2'-bipyridine) oxomolybdenum(IV) $[MoO(bpy)_2][PF_6]_2$ (2) – PPh_2Me (365 mL, 1.705 mmol) was added to a solution of $MoO_2(bpy)_2$ (300 mg, 0.682 mmol) in pyridine (40 mL). The reaction mixture was heated at reflux for 2 h. To the cooled solution was added $(Bu)_4N(PF_6)$ (544 mg, 1.40 mmol), and the solution stirred at RT for 2 h. The reaction was filtered. To remove excess pyridine, the solid was suspended in cyclohexane, and then the solvent was removed. This was repeated until pyridine was no longer detectable by NMR. The solid was then dried *in vacuo*. The product was isolated as a red–orange powder (208 mg, 43%).

bis(benzene-1,2-dithiolate) oxomolybdenum(IV) $[MoO(bdt)_2][NEt_4]_2$ (3) – $[MoOCl_5][PryH]_2$ was dissolved in dry ethanol with sodium metal. After 30 minutes, a solution of lithium benzenedithiolate in ethanol was added. The resultant solution was stirred for 1 hour. A solution of Et_4NCl in ethanol was added and the solution was allowed to stir for an additional hour. This precipitate was then filtered under nitrogen, washed with ethanol and dried *in vacuo*.

[40] R. R. Khojasteh, S. L. Saremi, and M. Ahmadzadeh, *Asian Journal of Chemistry* 2011, **8**, 3769-3770.

(1): FT–IR (KBr disk): 3078 (C–H), 1597(C=C), 1445 (C=C), 1055 (C–N), 913(Mo=O), 883 (Mo=O), 443, 420 cm^{-1}. ^{1}H NMR (400 MHz, DMSO): δ (ppm): 8.65 (d, 4H), 8.36 (d, 4H), 7.93 (t, 4H), 7.43 (t, 4H)

(2): FT–IR (KBr disk): 3048 (C–H), 1608 (C=C), 1449 (C=C), 1071 (C–N), 946 (Mo=O), 457, 434 cm^{-1}. $^{1}HNMR$ (400 MHz, $CDCl_3$): δ (ppm): 7.68 (d, 4H), 7.38 (d, 4H), 6.94 (t, 4H), 6.78 (t, 4H)

(3): FT-IR (KBr disk): 1483 (C=C), 1174 (C-C, C-S), 938 (Mo=O), 713 (C-S), Et_4Cl (2948, 1630, 1479, 1440.5, 1383, 1181, 1170, 1101, 790, 780) cm^{-1}. ^{1}H-NMR (400MHz, d_6-DMSO): δ (ppm) 7.3 (dd, 4H), 6.8 (dd, 4H), 3.16 (q, 8H), 1.12 (t, 12H)

Chapter 3: $[MoO(bpy)_2]^{2+}$ as a Hydrogen Evolution Catalyst

Characterization: Electronic and Vibrational Structure –

The complex bis(bpy) oxomolybdenum-(IV) **(2)** was prepared for use as a proton reduction catalyst. In addition to the recent appearance of high-valence oxomolybdenum compounds as proton reduction catalysts in the literature, the oxomolybdenum motif appears in several oxygen transfer enzymes and possesses multiple electron redox chemistry that makes it a promising candidate to catalyze the two-electron hydrogen evolution reaction.

$[Mo(bdt)_2O]^{2-}$ was synthesized as outlined in the experimental section. UV-vis and IR spectroscopy were used to examine the compounds electronic and vibrational structure; the two spectra are visible in *Figure 6*. The UV-vis spectrum features an intense $\pi^* \leftarrow \pi$ transition in the ultraviolet region of the spectrum, and a weak $^{1}MLCT$ transition (broad) centered at approximately 430 nm. The IR spectrum exhibits the

expected signals (which are assigned in the experimental section), but most notably, indicates the presence of the intense Mo-O stretching vibrational mode, which is excited at 946 cm^{-1}. This value is consistent with other oxomolybdenum (IV) compounds. The energy at which this vibrational mode is excited is used as an indicator of the Mo-O bond order and molybdenum oxidation state.

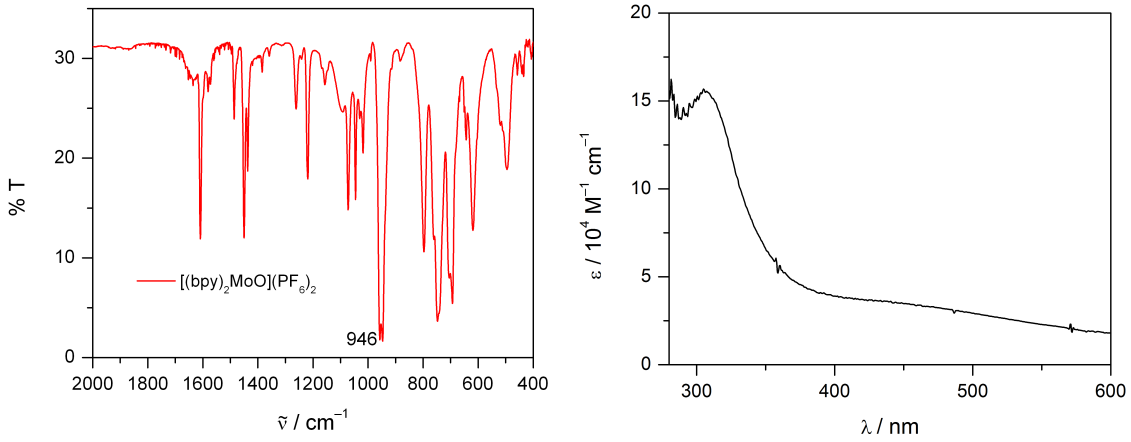

Figure 6. The IR spectrum of $[MoO(bpy)_2](PF_6)_2$ **(2)** was taken in a pressed KBR disk in an FT-IR spectrometer. The UV-vis spectrum of **(2)** was taken in DMSO with a catalyst concentration of 0.5 mM.

Electrochemical Studies –

Next, the catalyst was examined electrochemically. When dissolved in dry dimethyl sulfoxide (DMSO), the catalyst displayed no discernable electrochemistry (*Figure 7*). The only redox features visible in the cyclic voltammogram were the reversible reduction and oxidation of ferrocene, an internal standard, and the non-faradaic polarization of the electrode surface.[41] At the potential applied, there was not sufficient thermodynamic driving force to reduce the molybdenum (IV) complex in the absence of acid.

[41] Bard, A.J.; Faulkner, L.R. *Electrochemical Methods*; Wiley: New York, 2001, pp 15-17.

Upon addition of tosic acid, two reduction events appeared within the potential window of DMSO (see *Figure 8*). An irreversible wave appeared at -1.5 V vs $Fc^{+/0}$. This reductive wave is followed immediately by a large cathodic current that is assigned to the catalytic reduction of protons to dihydrogen. Notably, neither reductive wave had a corresponding oxidative wave on the positive potential sweep. For the catalytic wave at -1.75 V, this makes sense; this large wave represents the evolution of hydrogen gas, an irreversible process. One might expect to see an oxidative wave slightly positive of the reductive wave at -1.5 V, corresponding to the oxidation of the reduced complex back to the molybdenum (IV) state, **(2)**. There was no corresponding oxidative wave, implying that the reduction at -1.5 V was also irreversible. This irreversibility was attributed to the reduction being coupled to the complex accepting two protons from solution.

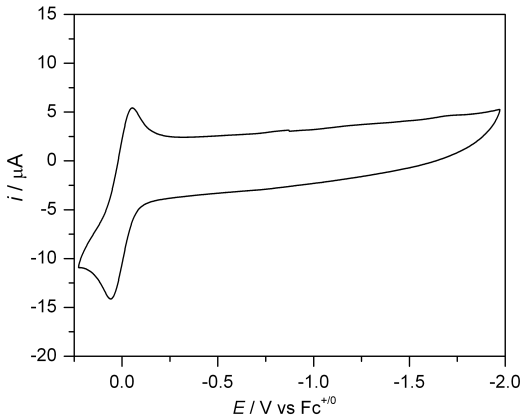

Figure 7. The cyclic voltammogram illustrates that in the absence of acid, there was no discernible redox chemistry within the potential window of DMSO. The redox wave present in the voltammogram was the internal standard, $Fc^{+/0}$.

To determine the overpotential required to evolve hydrogen at the catalyst, a cyclic voltammogram was taken of a solution of tosic acid in DMSO using a platinum electrode. The onset of cathodic current at platinum in DMSO is -0.80 V vs. $Fc^{+/0}$. This is a good estimate for the thermodynamic potential required for the hydrogen evolution reaction to proceed, as platinum is known to evolve hydrogen from acidic solutions with

minimal overpotential. Using this value, it was estimated that the $[MoO(bpy)_2]^{2+}$ catalyst evolved hydrogen with an overpotential of approximately 0.95 V.

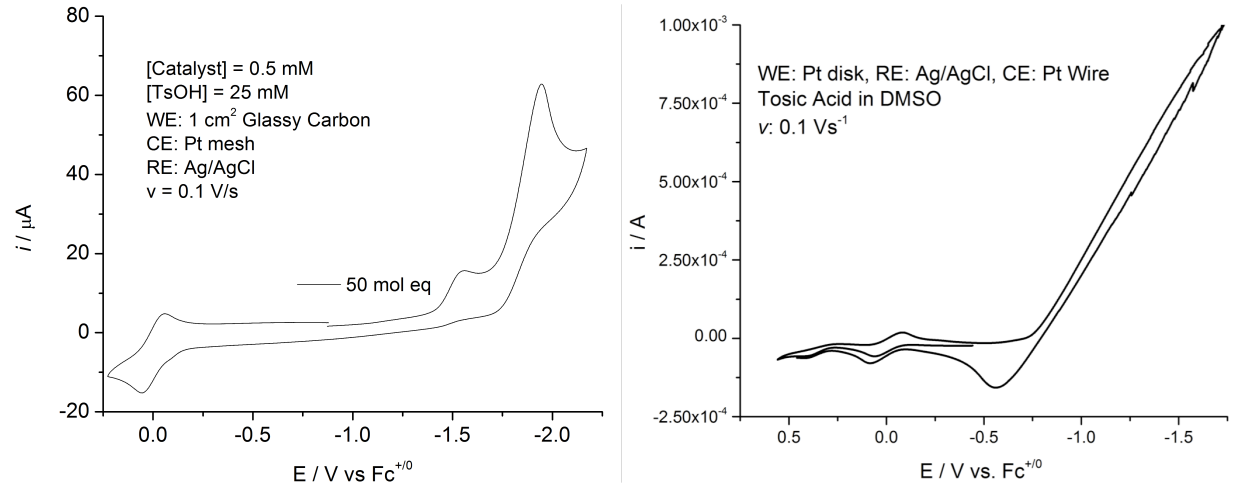

Figure 8. A typical cyclic voltammogram (left) of $[MoO(bpy)_2]^{2+}$ in the presence of tosic acid featured two reductive waves, one at -1.5 V vs. $Fc^{+/0}$, and a large catalytic wave with an onset of approximately -1.75 V vs. $Fc^{+/0}$. The true thermodynamic potential of proton reduction in DMSO from tosic acid was estimated to be -0.80 V vs. $Fc^{+/0}$, by taking a cyclic voltammogram (right) using a Pt working electrode. The overpotential at **(2)** was estimated to be 0.95 V.

To assure the catalyst was responsible for the currents observed, control experiments were performed. To show that hydrogen was not being evolved solely at the electrode, cyclic voltammograms similar to the one in the left half of *Figure 8* above were performed in the absence of **(2)**. The results are visible in *Figure 9*. There was a small background current representing thermodynamically favorable, but kinetically hindered reduction of protons at the glassy carbon working electrode. In a 25 mM solution of tosic acid, the current at -1.85 V was 5 times less in the absence of **(2)**, than with it present. This background current was subtracted from all chrono-coulometry experiments presented herein in order to represent an accurate value for the amount of hydrogen produced by the catalyst.

To assure that proton reduction was the source of the catalytic current, cyclic voltammograms of **(2)** were performed in the presence of increasing concentrations of tosylate anion ($NaTsO^-$). As shown in *Figure 9*, there was no faradaic current observed in the presence of **(2)** and tosylate anion. This strongly supports the assertion that both reductive waves in the voltammogram above needed protons to proceed.

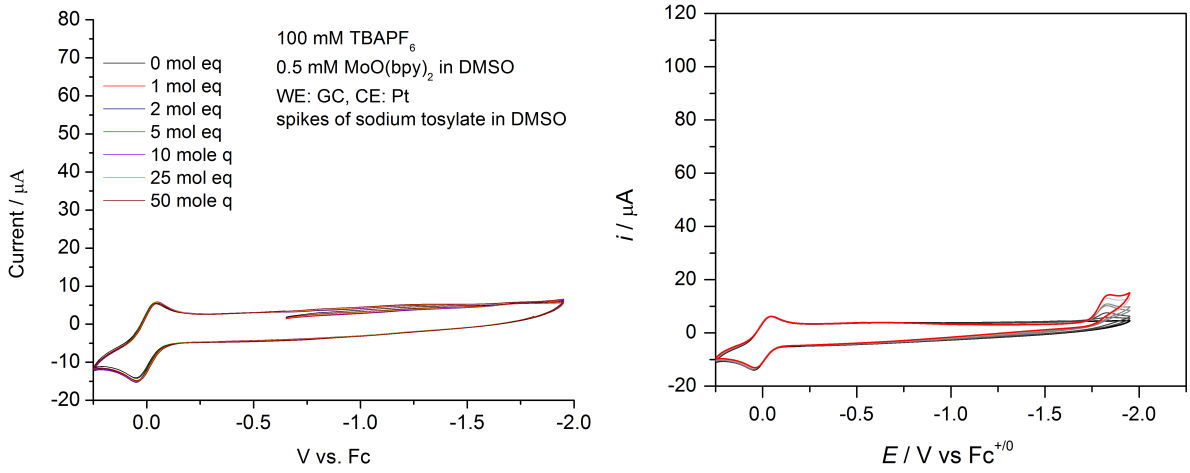

Figure 9. Cyclic voltammograms taken in the absence of **(2)** with increasing concentrations of acid showed minimal background current at the glassy carbon working electrode (right), ensuring that the catalyst was responsible for the large catalytic currents seen in *Figure 8* and *Figure 11*. Cyclic voltammograms taken in the presence of **(2)** with increasing concentrations of tosylate anion showed no discernable redox events, indicating that the protons in solution were responsible for the currents observed in solutions of **(2)** with tosic acid.

To accurately determine kinetic rate constants and other parameters, the diffusion coefficient, D_0, was determined for **(2)** using cyclic voltammetry. The diffusion coefficient is a constant that is characteristic of a specific molecule in a chemical environment that indicates how quickly the molecule diffuses in solution due to random motion, and has units $cm^2 \bullet s^{-1}$. The average distance a molecule travels from it's initial location after *t* seconds, the root-mean-square distance, $\overline{\Delta}$, is related to D_0 as indicated below:[42]

$$\overline{\Delta} = \sqrt{2D_0 t} \qquad \textit{Equation 1.}$$

[42] Bard, A.J.; Faulkner, L.R. *Electrochemical Methods*; Wiley: New York, 2001, pp 147.

A typical value for D_0 in aqueous solutions is 5 x 10^{-6} $cm^2 \bullet s^{-1}$. The diffusion coefficient is found by taking multiple cyclic voltammograms of the same solution at different scan rates. The peak current, i_p, in a cyclic voltammogram can be calculated via the equation:[43]

$$i_p = (2.69 \times 10^5) n^{3/2} A D_0^{1/2} C_0^* v^{1/2} \qquad \textit{Equation 2.}$$

where n is the number of electrons transferred in the redox event, A is the electrode area in cm^2, C_0^* is the initial concentration of the analyte in solution in $mol \bullet mL^{-1}$, v is the scan rate in $V \bullet s^{-1}$, and i_p is in amperes. Several voltammograms were taken at different scan rates in a solution containing **(2)** at a concentration of 0.5 mM, and tosic acid at a concentration of 40 mM. Notably, the acid was in large excess, so the diffusion process that limited the current at high potentials would be the diffusion of the catalyst to the electrode, not protons. The peak currents were recorded from these cyclic voltammograms and were plotted against the square root of the respective scan rates in *Figure 10* below.

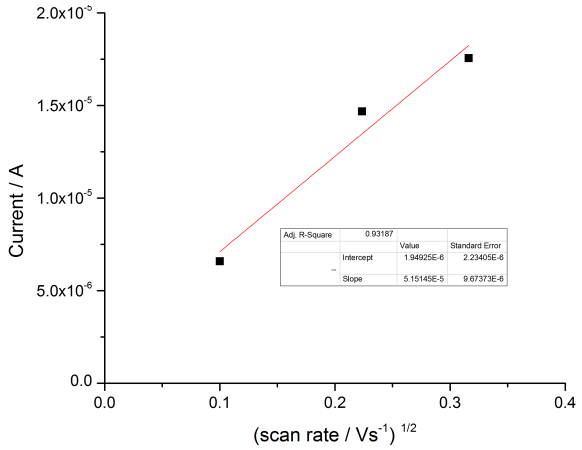

Figure 10. The peak currents for the reduction at -1.5 V vs. $Fc^{+/0}$, show a linear dependence with the square root of the scan rate, $v^{1/2}$, typical of a diffusion limited process. The slope of the linear dependence correlates to a diffusion coefficient of 1.5 x 10^{-7} $cm^2 s^{-1}$ for **(2)**, which is typical for small molecules in DMSO

The fit slope of the line was 5.2x10^{-5} ± 9x10^{-6} $A \bullet (V \bullet s^{-1})^{1/2}$. This slope represents all of the constants to the left of $v^{1/2}$ in the equation for i_p above. Using the equation, and the

[43] Bard, A.J.; Faulkner, L.R. *Electrochemical Methods*; Wiley: New York, 2001, pp 231.

experimental conditions (electrode area and starting concentration), the diffusion coefficient was calculated to be 1.5×10^{-7} $cm^2 \cdot s^{-1}$, a reasonable value **(2)** in DMSO.

Further electrochemical experiments were used to more thoroughly understand the reduction events represented by the two peaks in the cyclic voltammograms of **(2)** in the presence of tosic acid. To measure the proton-dependency of the first reductive wave at -1.5 V, the position of the reductive wave as a function of acid concentration was examined. The potential at which electrochemical reactions occur is determined by the Nernst equation. For the reaction $[Mo^{IV}]^{p+} + ne^- + kH^+ \rightarrow [Mo^{IV-p}H_k]^{p-n+k}$, the Nernst equation is:

$$E_{\exp} = E^{0/} + \frac{RT}{nF} \ln \frac{[Mo^{IV-p}H_k]}{[Mo^{IV}][H^+]^k}$$

Where *R* is the gas constant, *T* the temperature in Kelvin, *n* the number of electrons involved in the reaction, and *F* Faraday's constant. After computing the product of all of the constants and changing the base of the natural logarithm to 10, the equation becomes:

$$E_{\exp} = E^{0/} + \frac{0.059}{n} \bullet \log \frac{[Mo^{IV-p}H_k]}{[Mo^{IV}][H^+]^k}$$

Rearranging the equation using the properties of logarithms, yields the following expected pH dependence:

$$E_{\exp} = E^{0/} + \frac{0.059}{n} \bullet \log \frac{[Mo^{IV-p}H_k]}{[Mo^{IV}][H^+]^k} = E^{0/} + \frac{0.059}{n} \bullet \log \frac{[Mo^{IV-p}H_k]}{[Mo^{IV}]} - \frac{0.059k}{n} pH$$

This equation asserts that there should be a linear relationship between the reduction potential in solution and the solution's pH if the reduction is proton-coupled. Furthermore, the number of protons and electrons directly coupled to the reduction should be ascertainable from the slope of the line expressing this linear relation.

To explore this relationship, cyclic voltammograms were taken in solutions with 0.5 mM catalyst concentration, and varying concentrations of acid. The resultant cyclic voltammograms are plotted in *Figure 11*.

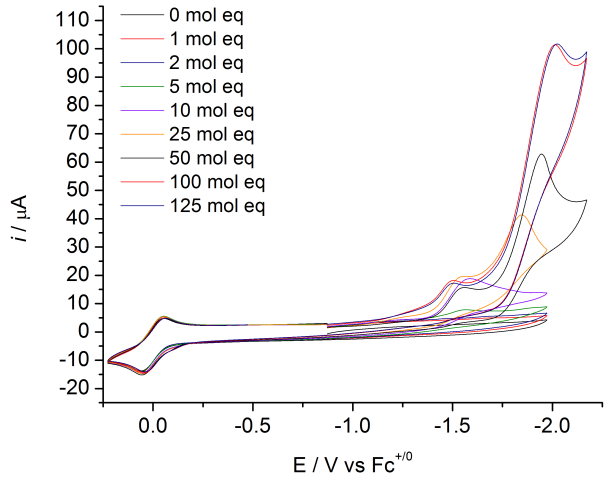

Figure 11. As more molar equivalents of tosic acid were added to the solution, the reductive wave at -1.5 V vs. $Fc^{+/0}$ shifted to more positive potentials and grew in quickly, limited by the diffusion of **(2)** to the electrode. The peak catalytic current continued to increase with tosic acid concentration until it leveled off at 100 molar equivalents of acid, limited by the turnover frequency at **(2)**

The potential derived in the Nernst equation usually refers to the reduction potential itself, $E_{1/2}$, the average of the peak currents in the cathodic and anodic scans. Because the reduction at -1.5 V vs. $Fc^{+/0}$ is irreversible, it is impossible to glean this value from the experimental data. There is an alternative: the half-peak potential, $E_{p/2}$:[44]

$$E_{p/2} = E_{1/2} + 1.09\frac{RT}{nF}\ at\ 25^{\circ}C \qquad \textit{Equation 3.}$$

The equation indicates that $E_{p/2}$ for a given solution should be shifted positive of $E_{1/2}$ (the quantity we are interested in) by a constant, independent of acid concentration. Thus, the linear relationship between $E_{1/2}$ and pH should be conserved between $E_{p/2}$ and pH. Furthermore, using $E_{p/2}$ solves many of the problems that would arise from using $E_{1/2}$. The use of $E_{p/2}$ does not require the presence of an oxidative peak current, and the $E_{p/2}$ is much more positive than $E_{1/2}$. This minimized the effect of the overlapping catalytic current on the accurate determination of the potential at which the initial reductive process occurs. For the cyclic voltammograms above, $E_{p/2}$ was determined in this same way: First the peak current associated with the initial reductive

[44] Bard, A.J.; Faulkner, L.R. *Electrochemical Methods*; Wiley: New York, 2001, pp 231.

wave was determined. Second, the background current prior to the catalytic wave was determined. The average of these two currents was the half-peak current associated with the half-peak potential, $E_{p/2}$.

The pH was calculated based on the pK_a of tosic acid in DMSO, 0.8 (K_a = 0.13), which asserts that given an unperturbed solution of tosic acid in DMSO, 30% of the tosic acid will have dissociated into H^+ and tosylate anion. With this assumption, pH was calculated using the equation:

$$pH = -\log(0.3 \bullet [Tosic\ Acid]_{added}) \qquad \textit{Equation 4.}$$

With pH calculated in this way, $E_{p/2}$ was plotted against pH to produce the Pourbaix diagram in *Figure 12*.

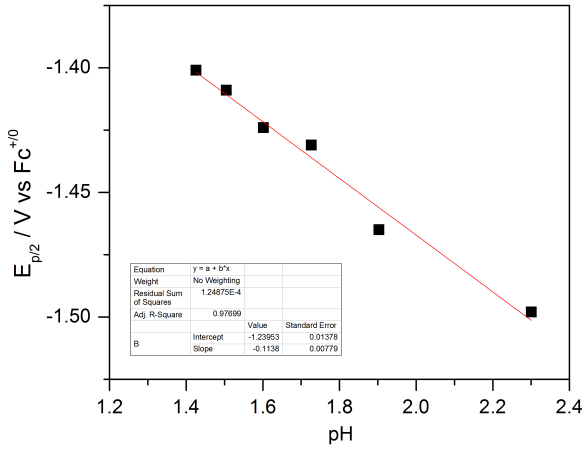

Figure 12. A Pourbaix diagram shows the linear dependence of the first reductive wave's half-peak potential, $E_{p/2}$, on pH. The half peak potential is related to $E_{1/2}$ by the addition of a constant, so if $E_{p/2}$ trends with pH, then so does the reductive potential, usually found as $E_{1/2}$. The slope of the linear dependence was found to be 114 ± 8 mV/pH consistent with a two-proton, one-electron process.

The slope was calculated to be 120 ± 8 $mV \bullet pH^{-1}$. This is in excellent agreement with a proton to electron ratio of two. This implies that the first reductive wave was coupled to two protonations at the catalyst. This is consistent with the fact that the initial reductive event didn't occur at all in the absence of acid, and that the position of the catalytic wave's initial rise in current was unchanging with changing acid concentration, indicating that the initial current in the second reduction was independent of protons in

solution. In a typical catalytic cycle, the catalyst was first simultaneously singly reduced and twice protonated, then reduced once more before eliminated hydrogen.

Kinetics Studies –

Next the kinetics of the catalytic reaction at **(2)** were examined. For a reversible electron-transfer reaction followed by a catalytic reaction, the peak catalytic current is given by the equation below:[45]

$$i_c = nFA[cat]\sqrt{Dk_{obs}} \qquad \textit{Equation 5.}$$

where *n* is the number of electrons required during one catalytic cycle, *F* is Faraday's constant, *A* is the electrode area, [*cat*] is the catalyst concentration, *D* is the diffusion coefficient of the catalyst, which is assumed to not change when the catalyst undergoes reduction and oxidation, and [*Q*] is the substrate concentration.

The derivation of the equation assumes that the substrate (acid) concentration is large enough to be considered constant on the time scale that the experiment is performed, that the reaction is first order in catalyst (which will later be shown to be reasonable), and that the reaction is diffusion limited to a planar electrode with a semi-infinite boundary condition.

More information about the kinetics of the reaction can be gleaned from varying substrate concentration by considering the Michaelis-Menten behavior of the catalyzed reaction on the time scales of the cyclic voltammetry experiments. Regardless of how complex the catalytic mechanism is, it can be simplified into the scheme below:

---

[45] (a) Bard, A.J.; Faulkner, L.R. *Electrochemical Methods*; Wiley: New York, 1980, pp 555-559. (b) Nichloson, R.S.; Shain, I. *Anal. Chem.* **1964**, *36*, 706. (c) Saveant, J.M.; Vianello, E. *Electrochim. Acta* **1965**, *10*, 905. (d) Appel, A.M.; DuBois, D.L.; DuBois, M.R. *J. Am. Chem. Soc.* **2005**, *127*, 12717.

$$MoO + 2e^- + 2H^+ \underset{k_r}{\overset{k_f}{\leftrightarrow}} MoOH_2 \xrightarrow{k_{cat}} MoO + H_2$$

Here k_{cat} is the rate at which the protonated and reduced complex releases H_2, the final, rate determining catalytic step. The rate constants k_f and k_r are not elementary reaction step rate constants, rather they are the gathered rate constants for the several elementary steps that constitute the formation and disassembly of the $MoOH_2$ complex that releases H_2. In particular, the catalytic steps implicit in k_f contain *at the least* 2 protonations and two reductions. If the applied potential at the working electrode is sufficiently negative, the two reductions will be fast. Because the peak catalytic currents occur at a potential far negative of the first reduction (the small reduction wave preceding the large catalytic wave), and even negative of the catalytic current onset, we may assume this to be the case. The protonation events are coupled to the fast and energetically driven reduction events. For these reasons, we may consider $k_f >> k_r$.

The Michaelis-Menten rate analysis below is based on the following assumptions: 1) We begin our cyclic voltammograms with no hydrogen in solution, the currents passed are relatively small, and the majority of the hydrogen generated will leave solution as a gas. These facts allow us to reasonably assume that $[H_2] << [H^+]$. 2) Our solutions contain many more molar equivalents of acid than catalyst, in other words, $[H^+] >> [MoO]$. 3) The concentration of protonated catalyst, $[MoOH_2]$ added to the concentration of unprotonated catalyst, [MoO] must equal the initial concentration of catalyst $[MoO]_0$: No catalyst is destroyed or added. $[MoO]_0 = [MoO] + [MoOH_2]$.

With the above Michaelis-Menten assumptions, *Equation 6*, containing the forward rate constant, k_f, and the rate constant for the twice protonated and reduced complex to eliminate hydrogen, k_{cat} can be derived (see the appendix).

$$i_c = nFA[cat]\sqrt{D\frac{k_f k_{cat}[H^+]^2}{k_{cat} + k_f[H^+]^2}} \qquad \textit{Equation 6.}$$

At low acid concentrations, *Equation 6* simplifies to:

$$i_c = nFA[cat]\sqrt{Dk_f[H^+]^2} = nFA[cat]D^{1/2}k_f^{1/2}[H^+] \qquad \textit{Equation 7.}$$

At high acid concentration, *Equation 6* simplifies to:

$$i_c = nFA[cat]\sqrt{Dk_{cat}} \qquad \textit{Equation 8.}$$

Using *Equations 7 & 8*, we can evaluate the kinetics of the catalyzed reaction by examining how the peak current changes with acid concentration. The peak currents of the multiple CV's in *Figure 11* were plotted against acid concentration in *Figure 13*. Notably, the peak current followed the trend expected upon adding additional acid. At low acid concentrations, the peak current had a linear relation to the amount of acid present as expected in *Equation 7*. This implies that the catalytic reaction was second order in acid. At high acid concentrations, the catalytic current ceased to increase with additional acid, indicating the acid independence expected in *Equation 8*. At higher concentrations that catalytic current was limited by the rate at which the complex could eliminate hydrogen, k_{cat}.

In the initial linear region, at low acid concentrations, the slope of the line of best fit was calculated to be $2.02\text{x}10^{-3} \pm 8\text{x}10^{-5}$ A•M_{acid}^{-1}. Using *Equation 7*, and the diffusion coefficient calculated earlier, the rate constant to prepare the catalyst to turn over hydrogen (to twice protonate and once reduce the complex in its resting state) was found to be 11,700 s^{-1} at -1.85 V vs. $Fc^{+/0}$. More interestingly, the rate constant for the elementary step to release hydrogen, k_{cat}, can be calculated from *Equation 8* using the turn-over limited current in the acid concentration-independent region of the left plot in

Figure 13, 2.08 x 10^{-5} A. Using this current, k_{cat} was calculated to be 1.24 s^{-1} at 25°C. These two rate constants indicate that the frequency of the complete catalytic cycle was significantly limited by the rate at which the catalyst released H_2. The fact that $k_{cat} << k_f$ can be at least partially justified in that the potential-dependent rate constants were examined near the observed potential for the process represented by k_{cat}, and far negative of the potential required for the processes represented in k_f.

Similarly, the dependence of the reaction on catalyst concentration was also examined by observing how the catalytic peak-current trended with increasing catalyst concentration at constant acid concentration. The peak currents were plotted against catalyst concentration (*Figure 13*, right), exhibiting a linear dependence. This linear dependence is expected in high and low acid concentration regimes, and indicates that the reaction was first order in catalyst concentration.

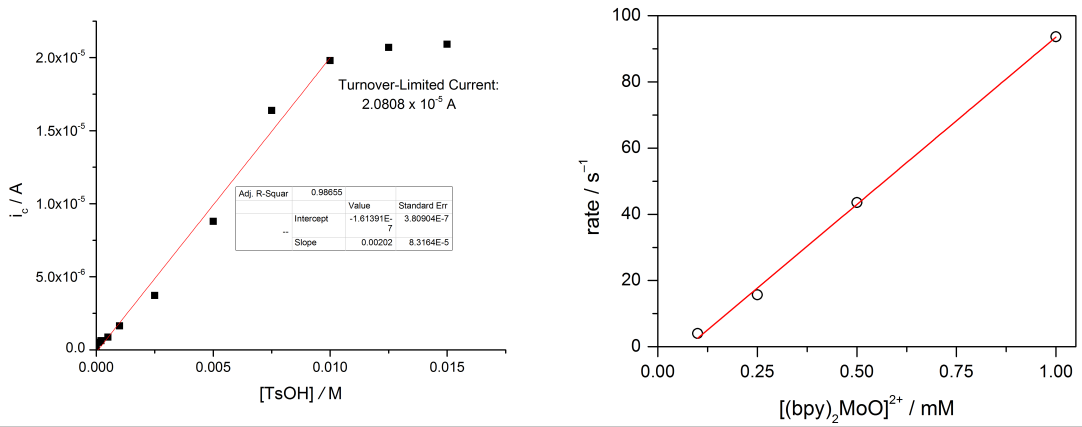

Figure 13. Plotting the peak catalytic current against acid concentration gave insight into the kinetics of the reaction (left). The initially linear slope indicated that the reaction is second order in acid concentration, as expected. The slope of the linear region of the plot, indicated that the rate constant to twice protonate and twice reduce **(2)** is 11,700 s^{-1} at -1.85 V vs. $Fc^{+/0}$. At higher acid concentrations, the peak current was limited by the rate at which **(2)** could release H_2, k_{cat}. The acid independent region of this plot corresponded to a k_{cat} = 1.24 s^{-1}. Plotting the peak catalytic current against concentration of **(2)** showed a linear (first order) dependence in **(2)** (right).

Steady State Behavior: Controlled Potential Coulometry and Detecting H_2 –

Controlled potential coulometry at -1.8 V vs. $Fc^{+/0}$ was used to probe the steady-state behavior of the reaction. The experiment was performed in an H-cell (see *Figure 14*, left) The working electrode was a strip of carbon felt, the reference electrode was Ag/AgCl. The plot in *Figure 14* shows the amount of charge passed against time with the background reaction occurring directly at the carbon felt electrode subtracted. Because it is difficult to buffer an organic, acidic solution, the bulk electrolysis was performed in a large excess of acid (100 molar equivalents). As expected from the kinetics studies, for the first three hours, the current was constant, as the current density is independent of acid concentration when there is a large excess of acid. This concentration independent behavior is exhibited in the linear portion of the plot (*Figure 14*, right) representing the first three hours. The linear increase of charge passed over time indicates a constant current. After the catalyst had consumed enough acid (evolved enough hydrogen), that the current density became dependent on acid concentration (the low concentration regime of the kinetics plots above), the current began to decay as the acid concentration went to zero.

In order to show that the decline in current was due to the consumption of the acid in solution, an additional 100 molar equivalents of tosic acid were added, and the original catalytic activity was immediately recovered, as indicated by the two linear regions in the plot below having the same slope. Notably, over the course of this experiment, the catalyst turned over nearly 100 molar equivalents of hydrogen with no discernable drop in catalytic activity. The solution was stirring in this experiment, so all

catalyst molecules realistically had access to the electrode surface. The controlled potential coulometry indicates that the catalyst is robust with a turnover number >> 100.

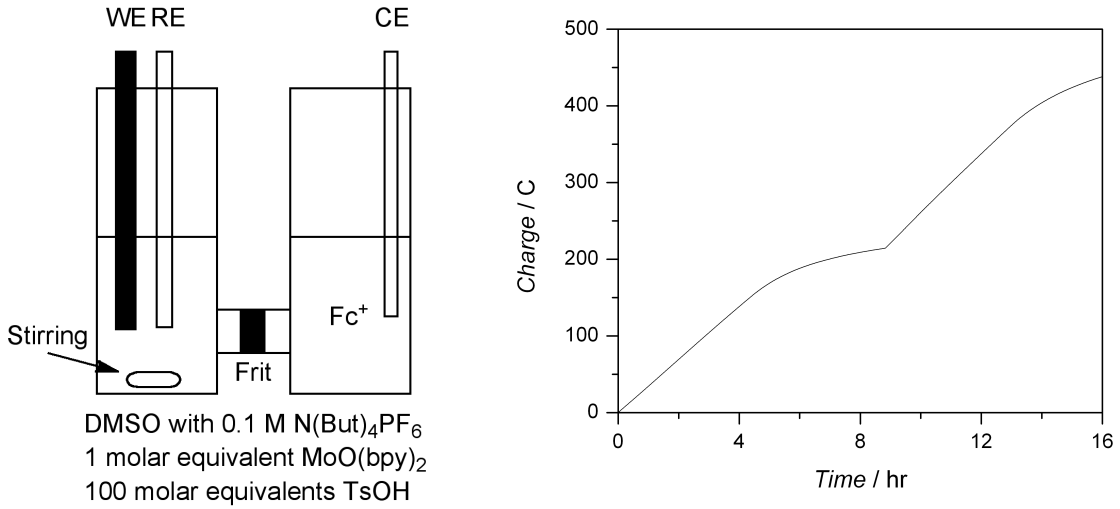

Figure 14. Controlled potential coulometry was performed at -1.8 V vs. $Fc^{+/0}$ in an H-cell with stirring (left) with 100 molar equivalents of acid. There were no signs of the degradation of **(2)**, as the current remainsed relatively constant over the first four hours. As all of the acid was consumed, the current began to decrease. The steady-state current (limited) by k_{cat} was regained in the presence of an addition 100 molar equivalents of acid.

Detecting H_2 –

Hydrogen was directly detected and measured by performing bulk electrolysis in an enclosed cell connected to an in-line mass spectrometer. The partial pressure of hydrogen in the headspace of the cell was measured by comparing the signal for hydrogen to the signals for N_2, O_2, and Argon. A representative three hour run is shown in *Figure 15* below. As expected, the N_2 signal dominates the minority gases. The inset shows the growth (zoomed-in) of the hydrogen signal relative to the small Ar and O_2 signals.

The chronocoulometry data from the three hours of bulk electrolysis was plotted along with the mass spectrometer's hydrogen quantification to ensure that all of the cathodic current passed in the cell was going towards H_2 evolution. In *Figure 16* below,

the choppy lines labeled “actual” represent the amount of H_2 produced over time as measured by the mass spectrometer. The smoother, “theoretical” lines represent the amount of hydrogen theoretically produced if each coulomb of cathodic charge passed went towards reducing protons. As can be seen in *Figure 16*, the theoretical and actual data trend together (ignoring the large amount of noise in the mass spectrometer data) indicating that all of the current passed in the cell reduced protons in solution.

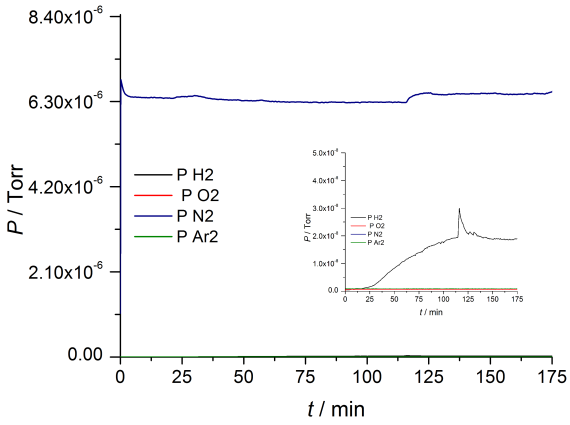

Figure 15. Controlled potential coulometry was performed with an in-line mass spectrometer. The mass spectrometer detected the partial pressure of H_2, using N_2 as an internal standard (the blue line). Hydrogen could be seen accumulating in the headspace of the cell in the inset, which shows an expanded view of the same data at low pressures.

At potentials sufficiently negative to reduce protons at the catalyst, there was a small background reaction at the surface of the carbon felt working electrode. In other words, some protons were reduced without the catalyst. In order to more accurately represent the amount of hydrogen evolved at the catalyst, a control experiment was performed in identical conditions, but in the absence of catalyst. The recorded current and mass spectrometer data were then subtracted from the data from the cell containing catalyst. The difference is visible in the right plot in *Figure 16*. The control data is the grey line in the left plot in *Figure 16*. The mass spectrometer was unable to accurately detect hydrogen at the small concentrations produced in the background reaction, as evidenced by the control data not initially trending with the current measured at the potentiostat. This artifact is visible in the subtracted data as well, but

at larger amounts of hydrogen, the actual and theoretical data still trend nicely. Over the course of three hours, each catalyst molecule in solution can account for 40 molecules of H_2 produced. In addition, each catalyst molecule turned over H_2 with an average frequency of 11.95 h^{-1}.

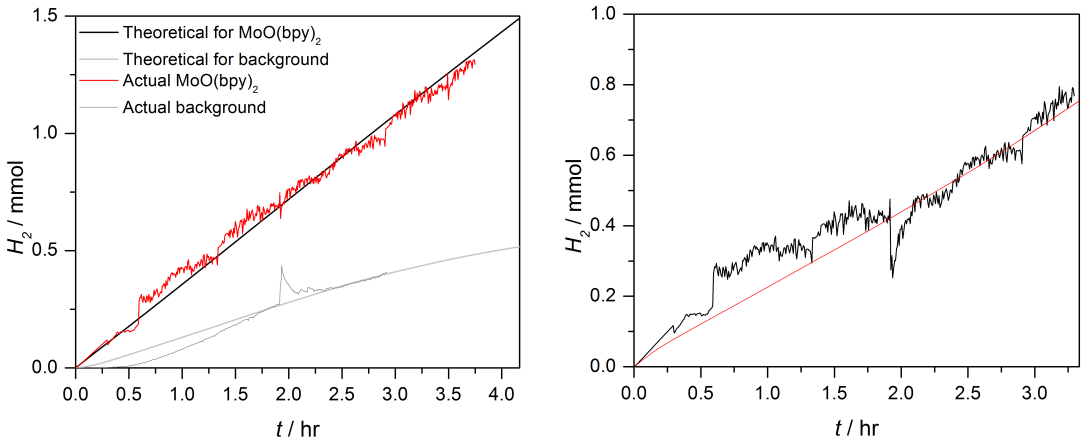

Figure 16. The amount of hydrogen detected by the in-line mass spectrometer (red, left) trended very well with the amount of charge passed measured by the potentiostat (black, left). To get a better idea of the amount of hydrogen evolved by the catalyst, the background current from a separate control experiment in the absence of catalyst was subtracted from the data on the left, yielding the plot on the right. The data from the potentiostat and mass spectrometer trended together even after subtracting the background current.

Electronic Structure: Spectroscopy and Computation –

Spectroelectrochemistry was used to examine the electronic structure of the catalyst in its resting state and during the catalytic cycle. Electrochemistry and spectroscopy were performed in a OTTLE cell using a mercury gold amalgam working electrode, Pt wire auxiliary electrode, and silver wire quasi-reference electrode. *Figure 17* below shows the evolution of the solution's absorption spectrum as the potential is scanned in the negative direction at a rate of 10 $mV \bullet s^{-1}$. Spectra were taken every ten seconds. The potential was taken far enough negative for the complex to evolve H_2.

The high-energy peak at 306 nm was largely unchanged even as cathodic current is passed. The fact that the $\pi^* \leftarrow \pi$ transition did not change upon reduction of the catalyst implies that the reduction was not ligand-based. This was corroborated by the band that grew in at 437 nm. The energy and molar absorptivity of this band were consistent with a metal to ligand charge transition (MLCT), indicating that the reduction was adding electron density to the molybdenum 4d orbitals. The set of spectra representing the reductive scan exhibited clean isosbestic points indicating that there were only two species being resolved on the time scale of the UV-vis experiments.

The band at 437 nm that grew in during the reductive can grew out during the oxidative scan, but did not completely disappear. This can be explained by considering the CV discussed earlier. At the beginning of the experiment, there was only $[Mo^{IV}O(bpy)_2]^{2+}$ in solution. As the potential was scanned sufficiently negative, the complex was once reduced and twice protonated as indicated by the Pourbaix diagram. The concentration of $[Mo^{III}O(bpy)_2H_2]^{3+}$ increased as the potential was scanned more negative. When the potential was sufficiently negative to evolve H_2, each complex that released H_2 returned to it's $[Mo^{IV}O(bpy)_2]^{2+}$ resting state, where it was once again quickly reduced and protonated. Based on the kinetic studies, the preparation of $[Mo^{IV}O(bpy)_2]$ was much faster than the step to release hydrogen from the complex at the potentials where hydrogen was released (very negative of the potential required to initially reduce and protonate the complex). As $[Mo^{IV}O(bpy)_2]^{2+}$ was consumed at the electrode, producing $[Mo^{III}O(bpy)_2H_2]^{3+}$, more $[Mo^{IV}O(bpy)_2]^{2+}$ diffused to the electrode from the bulk, allowing for the continued increase of the concentration of

$[Mo^{III}O(bpy)_2H_2]^{3+}$at the electrode, and the concurrent growth of the observed absorption at 437 nm.

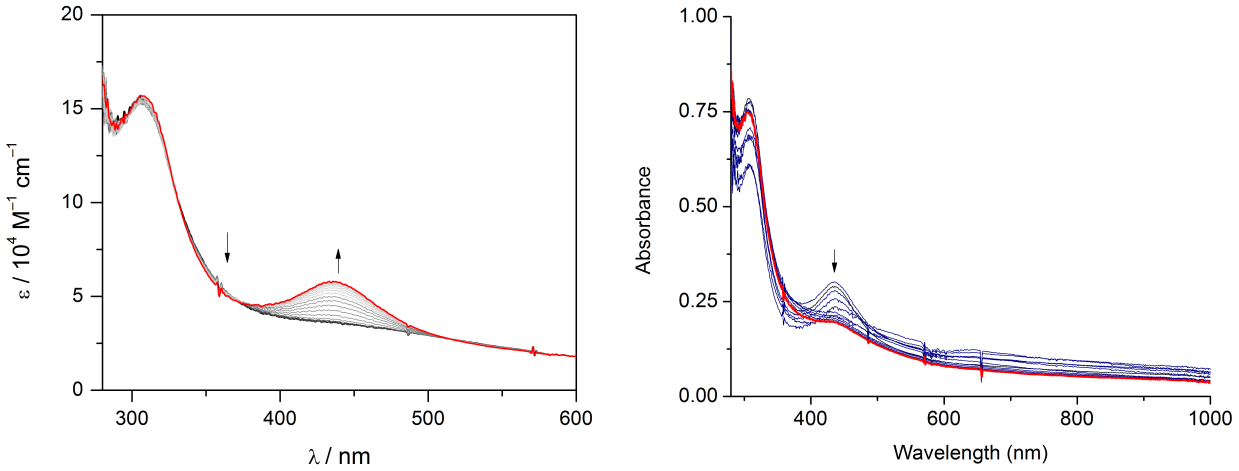

Figure 17. Upon scanning negatively (left), an intense ^{3}MLCT band grew in at 437 nm as the metal-based LUMO was populated. Clean isosbestic points indicated there were only two species absorbing in solution. During the oxidative scan (right), the band at 437 nm decreased, but did not disappear entirely. There were no longer clean isosbestic points. Spectra were taken through a thin film of solution surrounding a mercury-gold amalgam working electrode. Spectra were taken every 10 seconds, and the scan rate was 10 Vs^{-1}.

During the oxidative scan, eventually the potential was too positive for $[Mo^{III}O(bpy)_2H_2]^{3+}$ to turn over hydrogen. At this point, the majority of free $[Mo^{IV}O(bpy)_2]^{2+}$ had been consumed near the electrode, and the concentration of $[Mo^{III}O(bpy)_2H_2]^{3+}$ ceased to increase. $[Mo^{III}O(bpy)_2H_2]^{3+}$ then diffused away from the electrode. The band at 437 nm began to decrease, and there were no clean isosbestic points. A possible explanation for the lack of isosbestic points is that the net concentration of all Molybdenum species near the electrode decreased as $[Mo^{III}O(bpy)_2H_2]^{3+}$ diffused away from the electrode.

The reductive scan was started at open circuit potential, which in these solutions was approximately -0.5 V *vs*. Fc^+/Fc. *Figure 18* depicts the growth of the band at 435 nm (the increase in absorbance from the value observed at the beginning of the

experiment) against applied potential. The data corroborates the narrative above. At approximately -1 V *vs.* quasi reference electrode (-1.5 V *vs.* Fc^{+}/Fc), the absorbance began to increase. This was the potential at which the first, proton-coupled reduction occurred. The absorbance increased at a faster rate as the potential was swept negative and the current increased, and began to level off as diffusion of $[Mo^{IV}O(bpy)_2]^{2+}$ towards the electrode became slow.

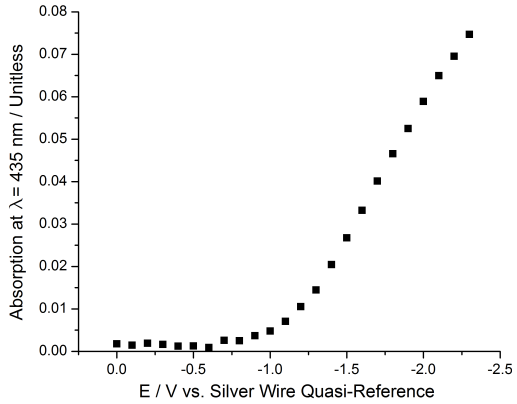

Figure 18. As the potential was swept more negative, the absorbnace at 435 nm began to increase at a potential corresponding to the first reduction at -1.5 V vs. $Fc^{+/0}$, and continued to increase linearly until very negative potentials, at which point it began to level off.

To assure that the observed spectroelectrochemistry was indeed due to the processes discussed, two controls were performed, and the results are displayed in *Figure 19*. The first control, the left plot represents the evolution of the solution over time without applying a potential. There were acid and catalyst present, but in the absence of a negative potential, no discernable chemistry occurred. Notably, these spectra match the spectrum of the catalyst in DMSO in the absence of acid indicating that protons do not interact with the complex in solution in the absence of an applied potential.

The second control experiment was analogous to the experiment in *Figure 17*, but in the absence of acid. As the cyclic voltammogram of the catalyst in the absence of acid in *Figure 7* would indicate, there was no qualitative change in the UV-vis

spectrum as the potential was swept negatively in the absence of acid. The slight fluctuations in the spectrum over time can be explained by slight changes in the chemical environment in proximity to the electrode do to non-Faradaic processes (redistribution of the electrolyte, solvent, and catalyst).

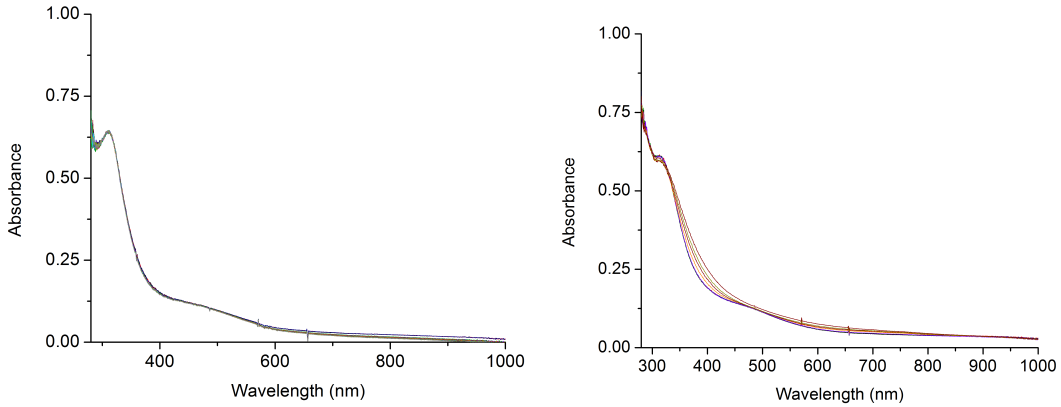

Figure 19. In the absence of an applied potential (left), there was no observed change in the UV-vis spectrum of **(2)**, indicating that the spectroelectrochemistry observed in *Figure 17* was not caused by the electrode alone. In the absence of acid (right), there was no observed change in the UV-vis spectrum of **(2)** even as the potential was cathodically swept. This was expected, based on the CV of **(2)**, which showed no redox chemistry in the absence of acid.

DFT was used to corroborate our electrochemistry, spectroscopy, and spectroelectrochemistry. Geometry optimization, electronic structure calculations, and TD-DFT were performed using the B3LYP functional and the LanL2DZ basis set augmented by d and f polarization functions. Geometry optimization calculations of **(2)** were verified by vibrational analysis. In addition, the calculated MoO stretching frequency is in good agreement (within 60 cm^{-1}) with the observed frequency, 946 cm^{-1}.

The calculated geometry placed the molybdenum center in the center of a pseudo-square-pyramidal ligand field. The bipyridine ligands were slightly skewed relative to eachother (presumably due to steric repulsion) indicating that **(2)** has C2 symmetry. The N-N-N-N dihedral angle in the optimized geometry was found to be 32°

(see *Figure 20* below), and the energy barrier for the bipyridine ligands to twist relative to one another (to pass between stereoisomers) was estimated (by molecular mechanics calculations) to be 86 $kJ \bullet mol^{-1}$, significantly greater than the amount of energy available to the complex at room temperature. The Mo-O bond distance was calculated to be 1.735 Å, consistent with other oxomolybdenum (IV) compounds. The average Mo-N bond distance was calculated to be 2.151 Å. The compound has been crystallized from DMSO/(Et_2O), producing single crystals that initially appeared suitable for x-ray diffraction. The crystals however, produced a smeared diffraction pattern, indicating a high degree of disorder, perhaps due to the solution containing a racemic mixture of the complex's two stereoisomers (right-handed and left-handed twisting of the bipyridyl ligands relative to eachother).

The calculated electronic structure of the compound is illustrated in the left half of *Figure 20*. The molecular orbitals with siginificant contribution from the molybdenum 4d and oxygen 2p atomic orbitals were displayed next to the frontier orbital energies to indicate the d-orbital splitting in the ligand field, and because they are relevant to catalysis. The C2 Mulliken symbols are placed next to the respective orbital energies.

The electronic structure corroborates the UV-vis spectroscopy and spectroelectrochemistry. The HOMO is ~75% metal based (from the atomic orbital coefficients), with TD-DFT indicating that the lower energy shoulder to the right of the high-energy $\pi^* \leftarrow \pi$ transition in the UV-vis spectrum is a ^{1}MLCT. The primarily ligand based excited state is calculated to have an energy of 2.87 eV (433 nm) with charge being transferred from the HOMO to a mixture of the LUMO+3 (64%), LUMO+2, LUMO+6, and LUMO+7 (10% each), each of which has significant ligand character.

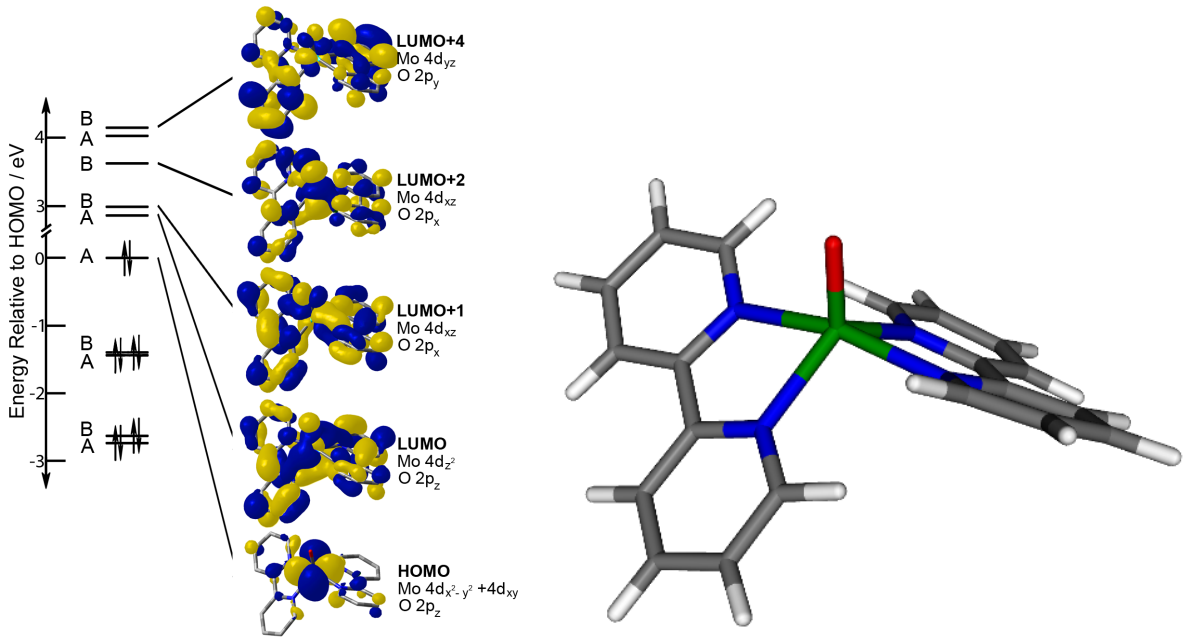

Figure 20. The optimized structure of **(2)** was calculated by DFT (LanL2dZ, B3LYP). The complex was predicted to have C2 symmetry, due to the steric repulsion between the two bipyridine ligands. To avoid repulsion, the ligands were predicted to twist relative to one another, producing screw-like stereoisomers (right). The barrier to convert between stereoisomers was estimated to be 86 kJ/mol by molecular mechanics calculations. The frontier orbital energies and Mulliken symbols are indicated (left). Molecular orbitals with significant Mo 4d character are also shown.

As the complex is reduced, the metal-based (11%) LUMO is populated, becoming the HOMO (singly occupied). This can be observed in the spectroelectrochemistry. The lower energy ^{3}MLCT grows in at 435 nm. From DFT, this relatively intense feature is also a metal to ligand charge transfer from the newly singly occupied orbital, labeled "LUMO" in *Figure 20* to the LUMO+5. The LUMO+5 is primarily ligand based, corroborating the assignment of the peak that grows in upon reduction as a MLCT transition. The MLCT in the reduced complex has a signifantly greater calculated oscillator strength than the MLCT in **(2)**, which is evident in the growing peak's large molar absorptivity coefficient.

Chapter 4: Electrocatalysis and Mechanistic Studies at $[MoO(bdt)_2]^{2-}$

Molybdenum-oxo Centers as Catalysts –

Molybdenum-oxo dithiolate motifs are present in many oxygen-transfer proteins' active sites.[46,47,48] Molybdenum in these proteins cycles between the Mo(IV) and Mo(VI) oxidation states. Their catalytic behavior is partially derived from the fact that the coordinating dithiolate ligands are highly non-innocent (i.e. donate charge to the molybdenum center), and participate in ligand-based oxidations. This behaviour is evident in electronic structure calculations of the $[MoO(bdt)_2]^{2-}$ **(3)**, the complex studied, in which the sulfur atoms (formally anions), are estimated to have a Mulliken charge of -0.13, and the "Mo(IV)" is calculated to have a Mulliken charge of +0.05, indicating that it is favorable for the ligands to donate electron density to the metal center. In addition, Molybdenum has rich redox chemistry; there are species with Mo(II,III,IV,V,&VI) oxidation states.[49] Although this catalytic motif has been widely studied as the site of oxidation and oxygen transfer reactions, the motif's multiple redox states and non-innocent coordination environment have not been examined for reductive catalysis.

With these considerations in mind, the $[Mo^{IV}O(bdt)_2](NEt_4)_2$ was synthesized as described in the experimental section, and was found to perform hydrogen evolution chemistry. The thermodynamics and kinetics of the catalytic cycle were studied with cyclic voltammetry, and the catalytic mechanism was investigated with spectroscopy coupled to electrochemistry.

---

[46] Hille, R. *Chem. Rev.* **1996**, *96*, 2757-2816.
[47] Romao, M. *Dalton Trans.* **2009**, *2009*, 4053-4068.
[48] Tenderholt, A.L; Wang, Jun-Jieh; Szilagyi, R.K.; Holm, R.H.; Hodgson, K.O.; Hedman, B.; Solomon, E.I. *J. Am. Chem. Soc.* **2010**, *132*, 8359.
[49] Barret, Jack *Inorganic Chemistry in Aqueous Solutions*, **Royal Chemistry Society**, 2003.

*Catalytic Activity at **(3)*** –

The molybdenum complex was evaluated as a proton reduction catalyst in acetonitrile using acetic acid as the proton source. *Figure 21* shows a cyclic voltammogram of the catalyst in dry acetonitrile.

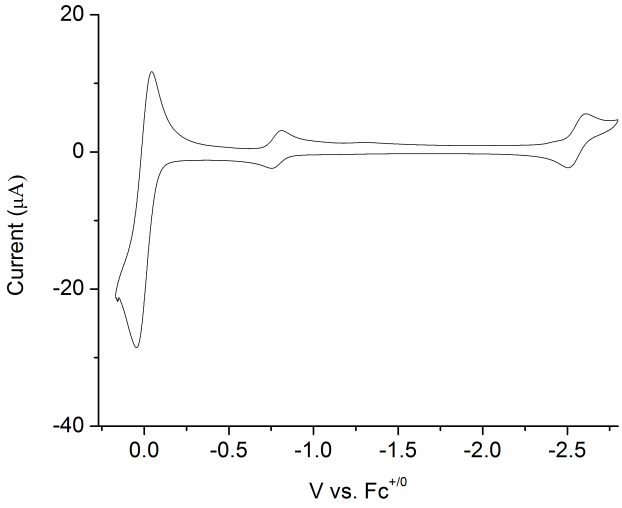

Figure 21. In dry acetonitrile, $[MoO(bdt)_2](Et_4N)_2$ was found to have two redox waves at -0.78 V and -2.56 V vs. $Fc^{+/0}$. These were assigned to the $Mo^{IV/III}$ and $Mo^{III/II}$ couples respectively.

The cyclic voltammogram and subsequent cyclic voltammograms in this section were taken with a glassy carbon disk working electrode, Ag/AgCl reference electrode, and platinum wire auxiliary electrode with $(NBu_4)(PF_6)$ as the supporting electrolyte. As the potential was scanned cathodically, there were two reversible reductions at -0.78 V and -2.56 V vs. $Fc^{+/0}$ corresponding to the Mo(IV/III) and Mo(III/II) redox couples respectively.

The left plot in *Figure 22* shows several cyclic voltammograms of **(3)** as acetic acid was spiked into the acetonitrile. As more acid was added, the first reductive wave was unchanged and unmoved at approximately -0.23 V vs. Ag/AgCl (-0.87 V vs. $Fc^{+/0}$) . The currents scans lay on top of eachother in this region regardless of acid concentration (*Figure 22*, left, inset). As the potential was scanned further negative, there was a small irreversible reductive current leading up to a large catalytic current

with onset near -1.25 V vs. Ag/AgCl (-1.89 V vs. $Fc^{+/0}$). Notably, this current was far positive of the second reductive potential in the scan in dry acetonitrile. In addition to being far positive of the original Mo(III/II) couple, the potential at which the catalytic wave appears, was acid-dependent. Analysis analogous to the Pourbaix analysis in **Chapter 3** indicates that the catalytic corresponded to a one-electron, 2-proton reduction, which as in agreement with the fact that the first reduction was proton independent. Again, to assure that proton reduction was occuring at the catalyst in solution, and not at the electrode, the same experiments were performed in the absence of catalyst at increasing concentrations of acid. These voltammograms, the right plot in *Figure 22*, show much smaller currents, and only at very negative potentials.

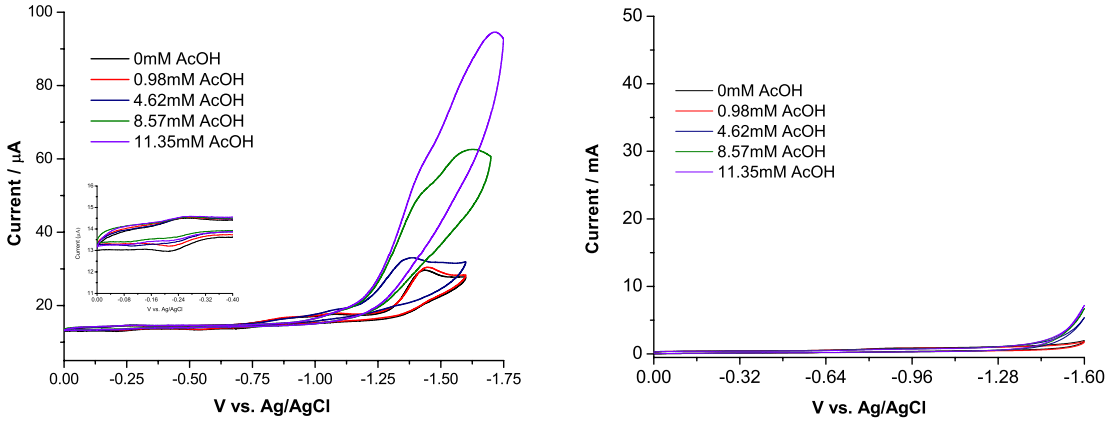

Figure 22. Upon adding acetic acid to a solution of **(3)** in DMSO, the $Mo^{IV/III}$ peak did not change, while a new, large catalytic wave grew in at approximately-1.89 V vs. $Fc^{+/0}$ (left). In the absence of **(3)**, the addition of acid resulted in significantly smaller currents at the glassy carbon disk working electrode (right).

Kinetic analysis, analogous to the analysis performed in **Chapter 3** for the $[MoO(bpy)_2]^{2+}$ complex **(2)** indicated that catalysis at $[MoO(bdt)_2]^{2-}$ was also second order in acid concentration and first order in catalyst concentration (see *Figure S1 and S2* in the appendix).

In order to corroborate the mechanistic insights gleaned from the electrochemistry, the mechanism was studied using several types of spectroscopy coupled to electrochemistry.

Spectroelectrochemistry (IR) –

IR spectroelectrochemistry was performed *in situ* in acetonitrile (wet) between two KBr plates. A miniature electrochemical cell was constructed to incorporate a small, thin piece of carbon felt as the working electrode, a small silver wire quasi-reference electrode, and a steel counter electrode that doubled as the injection port into the cell.

The counter electrode was carefully placed far from the the region of the cell probed in the spectrometer to avoid detecting products generated at the counter electrode. Prior to performing any spectroscopy, an initial CV was taken to establish the potentials of the two waves relative to the quasi-reference electrode. That CV is plotted in the left half of *Figure 23* below. Scanning cathodically from open circuit potential, there were two reduction events that are similar to those observed in the CVs in *Figure 22* above. There was an intial, reversible reduction followed by a large catalytic wave (indicating that the acetonitrile used was suffciently wet for the catalyst to evolve hydrogen. The voltammogram was an irregular shape not typically observed in cyclic voltammograms due to the carbon felt working electrode's unique geometry.

The right half of *Figure 23* below plots difference spectra that were taken as the cathodic voltages were applied above for 30 s intervals. The regions in the spectra that are left blank correspond to strong absorptions by acetonitrile, where the data was unsuitable for analysis. As the potential was held just negative of the first reduction wave (-0.5 V vs. the quasi-reference), two peaks grew in together around 3600 cm^{-1}.

These peaks are attributed to the increasingly nucleophilic oxo interacting noncovalently with C-H bonds. This assignment is made on the basis of the peak energies, shape, and the fact that the initial reduction was found to be independent of acid concentration in the analysis of the cyclic voltammograms in *Figure 22*.

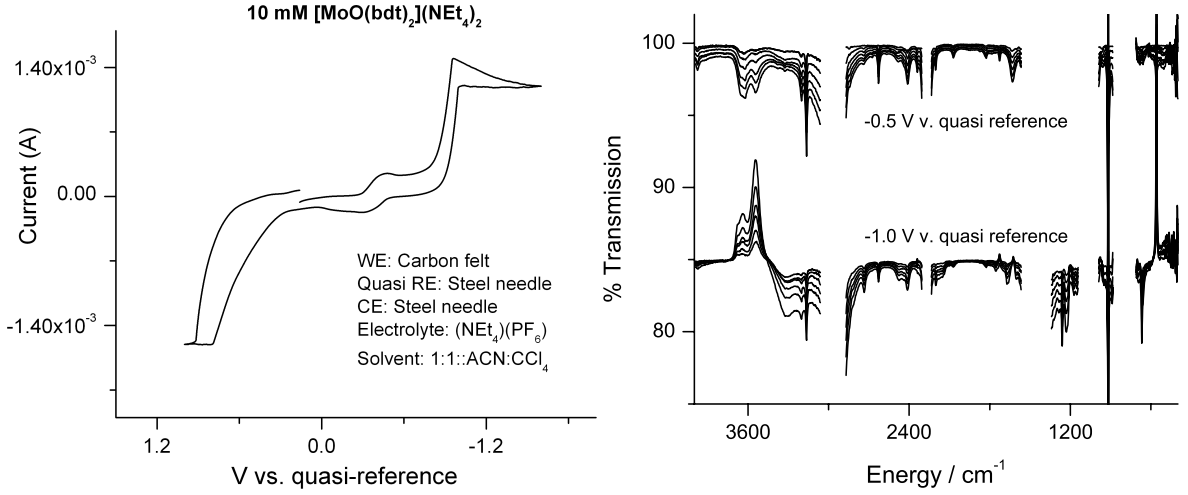

Figure 23. A make-shift three electrode electrochemical cell was constructed in a solution IR optical cell, producing the cyclic voltammogram on the left. Negative potentials were applied, and the difference spectra were plotted together to show absorbances growing in, and disappearing (right). Upon applying -0.5 V vs. the quasi-reference, two sharp peaks grew in at 3600 wavenumbers. Upon applying -1.0 V, those peaks dissapeared, and a broad peak grew in at 3300 wavenumbers accompanied, by a small, sharp peak at 2600 wavenumbers.

As the second, more negative (-1.0 V vs. the quasi-reference) potential was applied, the two peaks that grew in near 3600 cm^{-1} during the initial reduction disappeared, and a new, broad peak grew in at approximately 3300 cm^{-1}. In addition, a small peak near 2600 cm^{-1} grew in as well. This peak is more clearly visible in a spectrum taken of a higher concentration solution (80 mM) after a bulk electrolysis experiment was performed *ex situ*, and is attributed to the formation of an S-H bond.

Together, the spectra in *Figure 23* and *Figure 24* are consistent with the initial reduction being mostly metal-based. Based on DFT electronic structure calculations,

the LUMO of the initial complex is largely metal based. The LUMO features a π anti-bonding interaction between the Mo $4d_{xz}$ and O $2p_x$ atomic orbitals. Upon reduction, the LUMO was singly occupied, making the apical oxygen more nucleophilic. This nucleophilicity was responsible for the increased O-H-C interactions with solvent that were indicated by the increased absorption at 3600 cm^{-1}.

Upon the second reduction, the complex was twice protonated. The nucleophilic oxygen was protonated. This is evident in the disappearance of the peaks indicative of the unprotonated oxygen interacting with the solvent C-H bonds and in the appearance of the strong, broad absorbance at 3300 cm^{-1} (see the *Figure 23* above). There was also evidence that the second protonation occured at one of the basic sulfur atoms as evidenced by the peak near 2600 cm^{-1} growing in upon the second reduction. This sequence of events is consistent with the cyclic voltammograms in the *Figure 22*.

Further insight can be found from considering the electronic structure of $[Mo^{IV}O(bdt)_2]^{2-}$ calculated by DFT. The complex's LUMO is largely metal based, and features strong antibonding character between the molybdenum center and the apical oxygen and surrounding sulfur atoms. The O $2p_x$ and Mo $4d_{xz}$ orbital have a strong π anti-bonding interaction, while the S (in-plane) 3p orbitlas have a non-bonding/weak σ anti-bonding interaction. These characteristics of the LUMO are evident when looking at the twice reduced complex by IR. The double population of the anti-bonding LUMO corresponded to a weakening of the Mo=O and Mo-S bonds as evidenced by a shift of the Mo-O and Mo-S stretching frequencies to lower energies (see the *Figure 24* below). The weakening of the Mo=O bond and population of the oxygen 2p atomic orbital is also

consistent with the generation of a nucleophilic oxygen that at first interacted strongly with solvent C-H bonds and then received a proton from the acidic solution.

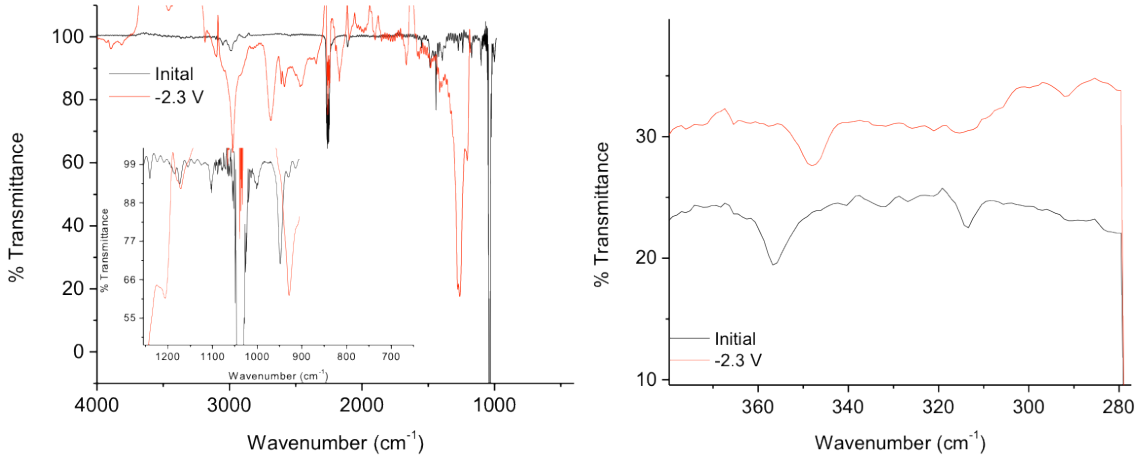

Figure 24. IR spectra of solutions collected after the bulk electrolysis of **(3)** at -2.3 V vs. $Fc^{+/0}$ in dry acetonitrile gave insight to where the electrons were going. The Mo-O stretching peak shifted to lower wave numbers (left, inset), reflecting the occupation of the anti-bonding, metal based LUMO. Similarly, the Mo-N stretching peak also shifted to lower wavenumbers (right).

Spectroelectrochemistry (EPR) –

To further examine the complex's LUMO, the complex was reduced in dry acetonitrile (*ex situ*), and the three solutions containing the Mo(IV), Mo(III), and Mo(II) species were examined by EPR spectroscopy. EPR spectroscopy studies species with unpaired electron(s), by placing the species in a magnetic field and probing the energy difference between states in which unpaired spins are aligned parallel and anti-parallel to the applied field by varying the field strength. Species have characteristic energy differences between states, which can be extracted from the field strength at which the sample absorbs a constant frequency radiation source.

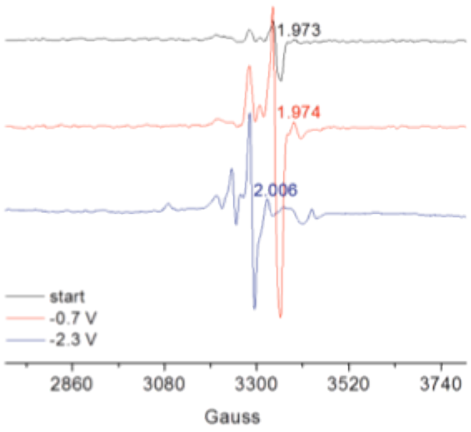

Figure 25. EPR spectra taken of solutions after bulk electrolysis of **(3)** in dry acetonitrile at -0.7 V and -2.3 V vs. $Fc^{+/0}$ indicated that the first reduction was primarily metal based, producing a spin 1/2 molybdenum (III) species as evidenced by the signal with a g value of 1.97. The second reduction was primarily ligand based, as indicated by the signal with a g value of 2.01, typical of an organic radical. The spectra of **(3)** (30mM) were taken in acetonitrile with 9.24 GHz light at a power of 20.45 mW. The spectra were taken at 77 K.

Figure 25 shows the Mo^{IV} (top), Mo^{III} (middle), and Mo^{II} (bottom) species' EPR spectra. The Mo(IV) species showed a very weak signal, which is expected, because the Mo(IV) species should not have had any unpaired electrons. Upon the first reduction, the signal at a g value of 1.974 grew significantly, which was characteristic of an upaired spin localized to the molybdenum center. This corroborated the IR data that suggested the first reduction populated the metal-based antibonding orbital. Upon the second reduction, the EPR signal shifted to a g value of 2, which indicated the formation of an organic radical. Again, this is consistent with mechanistic insight gathered from cyclic voltammetry and IR spectroscopy, which suggested that the second reduction was partially ligand based; the reduction increased the sulfurs' basicisity, promoting a second protonation at a sulfur site when there was a proton source present.

Spectroelectrochemistry (NMR) –

To further corroborate the nature of the two reductions, the same solutions examined by EPR were also examined with NMR spectroscopy. The complex's NMR spectrum contained two doublets of doublets (with chemical shifts of 7.43 and 6.92 ppm) indicating the complex's symmetry (see *Figure 26* below). After the first reduction, the peaks remained in nearly the same location, which was consistent with the first

reduction being primarily localized to the metal; the electron density near the ligands' protons was largely unperturbed. The second reduction hower shifted the two signals siginificantly. The signal with a chemical shift of 7.43 ppm was shifted downfield, while the signal with a chemical shift of 6.92 ppm was shifted upfield. This was consistent with the IR, EPR, and electrochemistry data that indicated that the second reduction was at least partially delocalized over the ligand framework.

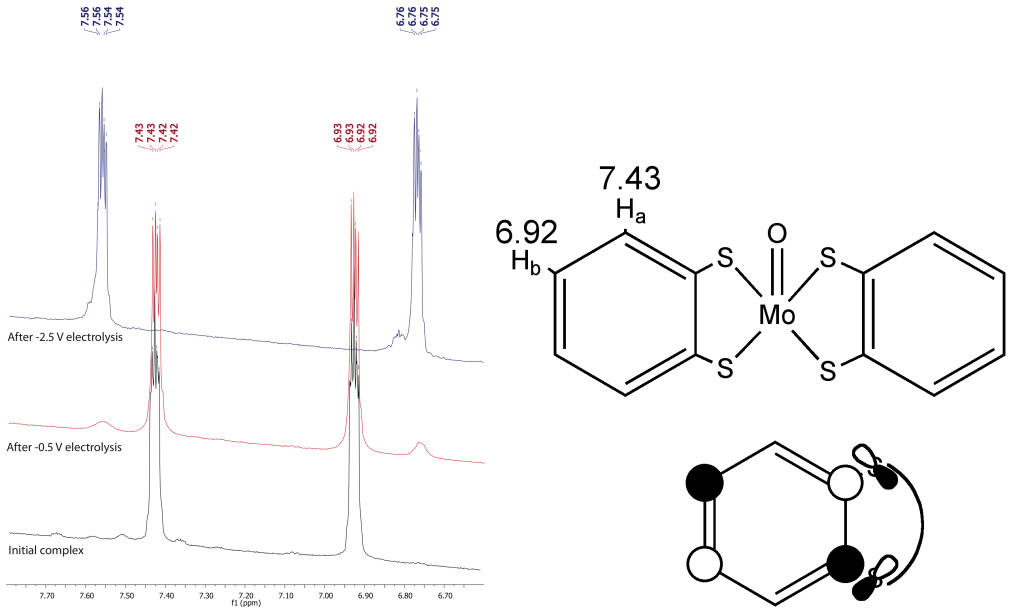

Figure 26. NMR spectra taken of solutions after bulk electrolysis of **(3)** in dry acetonitrile at -0.7 V and -2.3 V vs. $Fc^{+/0}$ were consistent with EPR and IR spectroelectrochemistry. The first reduction did not signicantly change the NMR spectrum, indicating that it was primarily metal based. Upon the second reduction, the peaks shifted, consistent with the formation of an organic radical. The peak assignments and the LUMO's π-system on the bdt ligand are indicated at the right to justify the new NMR shifts of twice reduced **(3)**.

The right half of *Figure 26* assigns the two NMR signals, and explaines the signals' shifts upon the second reduction. The diagram in the lower right shows the bdt portion of the catalyst's LUMO. There is a node at the carbons adjacent to the protons with chemical shifts of 7.43 ppm, and significant contribution from the $2p_z$ atomic orbitals of the carbons adjacent to the protons with chemical shifts of 6.92 ppm. The second

reduction further occupies the LUMO, adding electron density near the proton with a chemical shift of 6.92, shielding the proton from the magnetic field, shifting the 6.92 ppm signal upfield.

The mechanisitic insight found via the electrochemistry and spectroscopy above are used to propose the catalytic mechanism for hydrogen evolution at **(3)** diagrammed in *Figure 27* below.

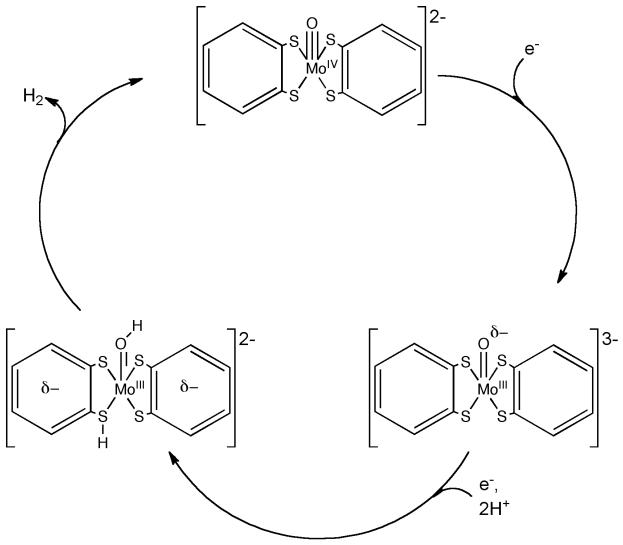

Figure 27. The spectroscopy and electrochemistry suggest the catalytic mechanism shown here. The initial complex is first reduced. The following reduction is a 2-proton, one-electron reduction, which protonates the nucleophilic oxygen and one of the basic sulfur sites. The complex them eliminates hydrogen, regenerating **(3)**.

Chapter 5: Developing a Molecular Device

Light Sensitizers –

$[Ru^{II}(bpy)_3]^{2+}$ is a d^6 complex with pseudo-octahedral symmetry (D_3). The ground state is $^1A_1$ with $(t_{2g})^6$ configuration in a strong ligand field. The lowest excited state is an excitation from a metal-based t_{2g} bonding orbital to a ligand-based t_{2g} π* orbital, a spin and symmetry allowed d → π* ^{1}MLCT in the visible region of the electromagnetic spectrum. Due to ruthenium's strong spin-orbit coupling, the singlet excited state can mix with the vibrational levels of a lower energy triplet excited state, allowing the system to quickly relax to a triplet excited state with very high efficiency. Return to the singlet

ground state from the triplet excited state is a spin-forbidden transition, the $^3T_1(t_{2g}^5e_g^1)$ excited state has a relatively long life time on the order of a microsecond.

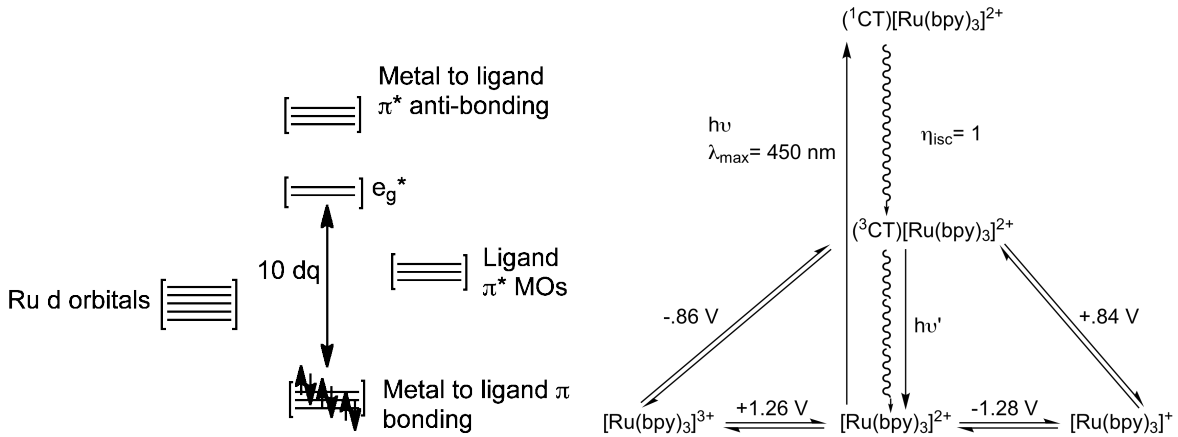

Figure 28. In a *tris*-bipyridyl ligand field, the ruthenium d orbitals with t_{2g} symmetry form bonding and anti-bonding orbitals with the bipyridyl π* orbitals (which also have t_{2g}) symmetry (left). The bonding molecular orbital is closer in energy to the metal d orbitals, and is primarily metal based. The anti-bonding molecular orbital is closer in energy to the bipyridyl π* orbitals, and is ligand based. The transition from the bonding to anti-bonding generates an oxidizing Ru(III) center, and reducing bpy^- radical. This long lived excited state (μs), is more easily oxidized and reduced than the complex in its ground state. This is reflected by the ground state and excited state reduction potentials shown on the right.

From this ^{3}MLCT state, the complex can perform redox chemistry. As illustrated in *Figure 28* above, the excited complex is simultaneously a strong oxidant and reductant; the ruthenium center is temporarily an oxidant, while the excited electron generates a reducing radical localized to a bipyridyl ligand.

This long lived excited state can be used in solar energy conversion schemes ranging from photocatalysis[50,51] to (more popularly) dye-sensitized solar cells.[52,53]

[50] Ozawa, H.; Haga, M.; Sakai, K. *J. Am. Chem. Soc.* **2006**, *128*, 4926.
[51] White, T.A.; Higgins, S.L.; Arachchige, S.M.; Brewer, K.J. *Angew. Chem. Int. Ed.* **2011**, *50*, 12209.
[52] Vlachopoulos, N.; Liska, P.; Augustynski, J.; Grätzel, M *J. Am. Chem. Soc.* **1988**, *110*, 1216.

These systems use the charge transfer that occurs upon excitation in ruthenium polypyridyl complexes to convert solar energy into chemical and electrical energy respectively. Ruthenium polypyridyl complexes have been extensively studied for their unique photophysical properties that make them useful for solar energy conversion applications.

The highly-efficient, dye-sensitized solar cell developed by Michael Grätzel illustrates a large advantage of ruthenium polypyridyl complexes as light-sensitizers in these systems. The absorption, emission, and absolute orbital energies in these complexes can be highly tuned by using different bipyridyl derivatives in place of unsubstituted bipyridine, and by replacing bipyridine with monodendate ligands. For example, the table below shows that exchanging one bipyridyl ligand for two strongly sigma-donating or π-acidic ligands can affect the properties mentioned above. [54]

		emission max (nm)		emission lifetime τ (ns)			E^0/V
Complex	**abs max (nm) (ε/10^4 $M^{-1}cm^{-1}$)**	**at 298 K**	**at 125 K**	**at 298 K**	**at 125 K**	**ϕ(%) at 125 K**	**(SCE)**
$[RuL_2(NCS)_2]$	534 (1.42), 396 (1.40), 313 (3.12)	755	718	50	960	0.40	0.85
$[RuL_2(CN)_2]$	493 (1.45), 365 (1.20), 310 (3.90)	702	700	166	1123	1.5	1.16
$[RuL_2Cl_2]$	534 (0.96), 385 (1.01), 309 (4.13)		800		105	0.074	0.57
$[RuL_2Br_2]$	530 (0.84), 382 (0.80), 309 (2.30)		750		110	0.26	0.56
$[RuL_2I_2]$	536 (0.68), 384 (0.66), 310 (2.50)		755		111	0.15	0.56
$[RuL_2(OH_2)_2]$	500 (1.19), 365 (1.09), 306 (4.90)		703		165	0.30	0.56

The absorption maximum and extinction coefficient can be tuned by altering the ligands about ruthenium. These characteristics determine what region of the solar spectrum the complexes can absorb, and how much material is needed to absorb the light. The emission maximum represents the energy available to do photochemistry

[53] O'Regan, B.; Grätzel, M. *Nature* **1991**, *353*, 737.
[54] Nazeeruddin, M.K.; Kay, A.; Rodicio, I.; Humphry-Baker, R.; Muller, E.; Liska, P.; Vlachopoulos, N.; Grätzel, M. *J. Am. Chem. Soc.* **1993**, *115*, 6382.

from the excited state, and a long emission lifetime is necessary to ensure that the desired photochemistry can occur on the time-scale allowed by the excitation lifetime. All of these characteristics are highly tunable as evident in the table above. For example, the empty π* orbitals of CN and NCS ligands allow for π-backbonding in the $[RuL_2(CN)_2]$ and $[RuL_2(NCS)_2]$ complexes, shifting the Ru(III/II) couple significantly positive. An optimal combination of these three tunable characteristics can drastically increase solar-to-electrical conversion efficiencies; the thiocyanate complex contributed to an overall solar-to-electrical conversion efficiency of 10%.

With these considerations in mind, several ruthenium polypyridyl complexes were synthesized as light sensitizers to be used in a supramolecular photocatalytic system. To alter the complexes' absorption and emission properties, several substituted bipyridine (4,4'-R-2,2'-bipyridine) derivatives were synthesized. Synthetic targets were selected in order to produce a series of ligands with a range of electron-donating and withdrawing character. The series of ligands synthesized is presented in *Figure* 29 below. The synthetic procedures used are referenced in the experimental section above.

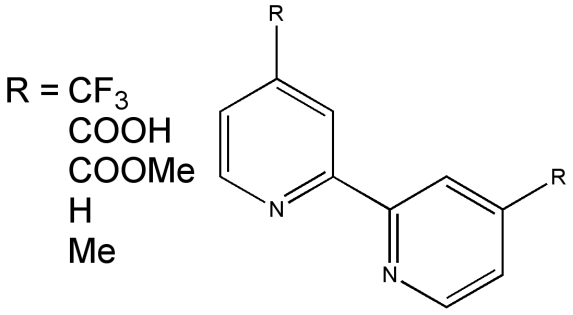

Figure 29. 2,2'-bipyridyl ligands substituted at the 4 and 4' position were synthesized in order to perturb the reduction potential, absorption spectrum, and emissive state in *tris*-bipyridyl complex, to design a complex suitable for use as a light sensitizer in a molecular photocatalytic device.

The trends expected for electron-donating, and electron-withdrawing substituted bipyridyl ligands relative to the unsubstituted ligand are summarized in the table below. The $Ru^{III/II}$ reduction potential in Ruthenium complexes with these substituted ligands

will show similar trends to the **(R-bpy)/(R-bpy^{-}•)** reduction potential. Electron withdrawing groups will facilitate R-bpy←Ru π-backbonding, which will withdraw electron density from ruthenium, making the metal center easier to reduce. The opposite is true of electron donating groups. Although mixed complexes show absorptions for excitations to each ligand, they emit solely from the lowest energy triplet excited state (localized to the lower energy R-bpy π* orbital). Such behavior can be used to spatially direct the emissive (reactive) excited state. Complexes with two bipyridyl ligands substituted with electron-donating groups and one ligand substituted with electron-withdrawing group for example will feature an excited state, in which the electron is localized to the EWG-substituted ligand. Such spatial control of the excited state is advantageous for designing molecular devices to do photocatalysis.

R-Group Type	**(R-bpy)/(R-bpy^{-}•) Reduction Potential**	**R-bpy π* Orbital Energy**	**(R-bpy)←Ru Transition Energy**
EWG	Made more positive	Decreased	Decreased
EDG	Made more negative	Increased	Increased

In addition to acting as strong electron withdrawing groups, the carboxylate groups on bipyridine also have the potential to bind to a ruthenium complex to an electrode surface. In the dye-sensitized solar cells mentioned above, ruthenium polypyridyl dyes are interfaced with nano-porous TiO_2 in this fashion.

An example of the effects of ligand substitution can be seen in the absorption spectra below in *Figure 30*. The plot shows the absorption spectra of $[Ru(bpy)_2Cl_2]$ and [Ru(4,4'-dimethyl-bpy)$_2$Cl$_2$]. The ^{1}MLCT absorption band in $[Ru(bpy)_2Cl_2]$ is redshifted about 100 nm relative to the ^{1}MLCT band in $[(bpy)_3Ru]^{2+}$. The σ-donating chloride ions donate charge the ruthenium center, stabilizing the MLCT excited state. The ^{1}MLCT band is even further redshifted (50 nm) in the methyl-substituted complex. This can be

justified by examining the molecular orbital diagram in *Figure 28*. The electron-donating methyl substituents destabilize the π* orbital, raising its energy relative to the ruthenium d orbitals. This decreases the bonding interaction between t_{2g} d orbitals and the ligand π* orbitals, decreasing the energy gap between the bonding and anti-bonding molecular orbitals, resulting in a lower energy ^{1}MLCT transition.

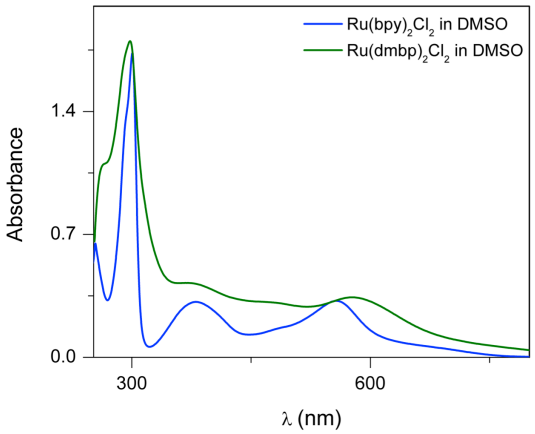

Figure 30. The spectra of $[(4,4'\text{-dimethyl-}2,2'\text{-bpy})_2RuCl_2]^{2+}$ and $[(bpy)_2RuCl_2]^{+}$ illustrate the ability to redshift the ^{1}MLCT transition by synthetically altering the bipyridyl ligands. Such substitutions can also affect the emission wavelength, and $Ru^{III/II}$ reduction potential.

Molecular Devices in the Literature –

The formation of dihydrogen from two protons is a two-electron process, but most excitations generate single-electron excited states. For this reason, it is difficult to perform multi-electron photochemistry at a single molecule acting as an absorber and catalyst. A strategy to mitigate this problem is to use a multi-component system.[55] One of the earliest systems to successfully photocatalytically evolve hydrogen fit into three-component scheme represented in the *Figure 31*.

This three component system uses a redox mediator, *M*, to collect excited electrons from the sensitizer, *S*, and shuttle them to the catalyst. The mediator carries multiple reducing equivalents to the catalyst with energy sufficient to reduce protons generated by the sensitizers' single-electron excited states. The textbook example of

[55] Esswein, A.J.; Nocera, D.G. *Chem. Rev.* **2007**, *107*, 4036.

such a system uses $[Ru^{II}(bpy)_3]^{2+}$ as the sensitizer, methylviologen as the redox mediator, and colloidal platinum as the catalyst.[56]

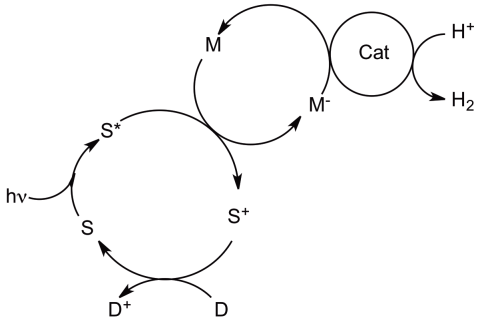

Figure 31. In a typical three-component system, the light sensitizer, *S*, is excited. The excited sensitizer, *S** then reduces a redox mediator, *M*. The reduced mediator, M^-, then reduces the catalyst, which collects multiple redox equivalents in order to perform a multi-electron reduction. The oxidized sensitizers, S^+, is reduced by a sacrificial donor, *D*, to regenerate *S*.

A strategy to eliminate the redox mediator and colloidal catalyst is to integrate the three components of the above system into a single molecular device, such as the ones pictured in *Figure 32* below.[57,58]

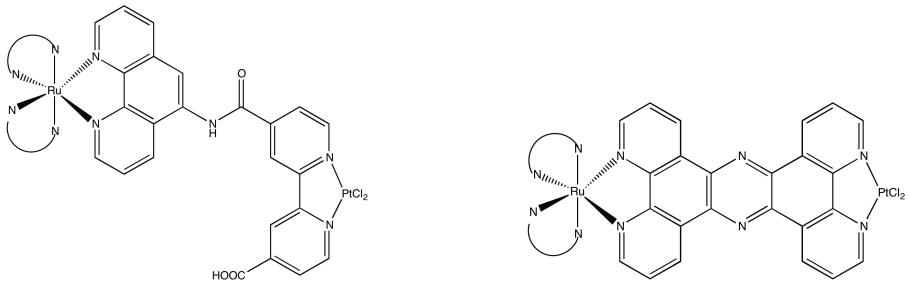

Figure 32. In these literature examples of molecular devices, a sensitizers, $Ru(bpy)_2$, is covalently attached to a catalytic site, $PtCl_2$, by a highly conjugated, conducting bridging ligand. The ruthenium polypyridyl complexes' ^{3}MLCT excited state relaxes to a ^{3}MMCT state, where the electron resides on platinum, allowing it to reduce protons. This system requires to molecules to evolve hydrogen.

Molecular devices utilize metal-to-metal charge transfers (MMCT), which have been studied extensively in homometallic systems.[59,60] Mixed-metal compounds were

[56] Moradpour, A.; Amouyal, E.; Keller, P.; Kagan, H. *Nouv. J. Chem.* **1979**, *2*, 547.
[57] Ozawa, H; Haga, M.-A.; Sakai, K. *J. Am. Chem. Soc.* **2006**, *128*, 4926.
[58] Rau, S.; Shafer, B.; Gleich, D.; Anders, E.; Rudolph, M.; Friedrich, M.; Gorls, H.; Henry W.; Vos, J.G. *Angew. Chem., Int. Ed.* **2006**, *45*, 6215.
[59] Creutz, C. *Progr. Inorg. Chem.* **1980**, *30*, 1.
[60] Hush, N.S. *Progr. Inorg. Chem.* **1967**, *8*, 391.

found to exhibit MMCTs that generated stable species, and have since been explored in the context of molecular devices capable of photochemistry. The barrier for electron transfer is high enough, that after a photoinitiated MMCT there is not enough energy at room temperature for the electron to transfer back.[61,62] In other words, MMCTs in heterometallic compounds produce stable excited states capable of photochemistry.[63]

A Molecular Photocatalyst: Excited State Energetics –

Future work will attempt to utilize MMCTs by coupling ruthenium polypyridyl sensitizers to a $[Mo^{IV}O(bpy)_2]^{2+}$ core that has been studied extensively as a proton reduction electrocatalyst to create a molecular device. Upon excitation, the ruthenium polypyridyl sensitizers will multiply reduce the molybdenum core, initiating evolution of H_2 in an acidic solution. The molecular device targeted is the supramolecular system illustrated in *Figure 33*.

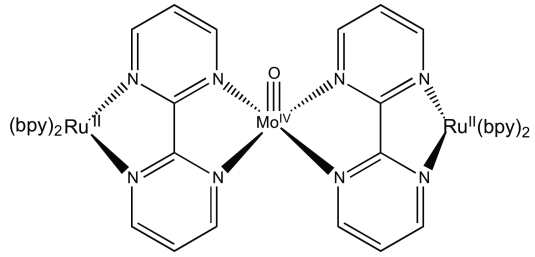

Light Sensitizer	Bridging Ligand	Catalytic Site

Figure 33. Our molecular device will be analogous to the systems presented in *Figure 32.* Each $Ru(bpy)_2$(2,2'-bipyrimidine) will act as the sensitizer, photoreducing the central molybdenum. The $MoO(bpym)_2$ active site will hopefully evolve hydogen upon reduction, analogously to **(2)** in the third chapter.

The desired chemistry of this system is illustrated in *Figure 34* below.[64] The ruthenium polypyridyl center will absorb visible light, exciting an electron from ruthenium to one of the ligands. The photogenerated ^{1}MLCT state will relax to the lowest energy

[61] Volger, A.; Osman, A.H.; Kunkley, H. *Coord. Chem. Rev.* **1985**, *64*, 159.
[62] Volger, A.; Kunkley, H. *Ber. Bunsenges. Phys. Chem.* **1975**, *79*, 83
[63] Volger, A.; Kunkley H. *Ber. Bunsenges. Phys. Chem.* **1975**, *79*, 301.
[64] Masanari, H.; Shigeyuki, M.; Sakai, K *Dalton Trans.* **2011**, *40*, 3973.

^{3}MLCT state via efficient intersystem crossing, facilitated by ruthenium's spin orbit coupling. The lowest lying charge transfer state is expected to be the $Ru^{III}(bpym^{-}\bullet)$ state (i.e. the electron is localized on bipyrimidine).[65] The bpy/bpy^{-}• and bpym/bpym^{-}• redox potentials indicate that bipyrimidine's π* is lower in energy than bipyridine's. From this ^{3}MLCT(bpym) state, the electron further relaxes to the ^{3}MMCT state, effectively photoreducing molybdenum so that the $[MoO(bpym)_2]$ motif can catalyze the two-electron hydrogen evolution reaction. Adding legitimacy to this scheme, $Ru(bpy)_2(bpym)$ light sensitizers have recently been used successfully to promote photocatalysis at a second metal center.[66]

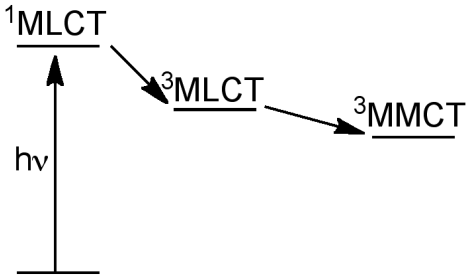

Figure 34. Visible light will excite the spin-allowed ^{1}MLCT in the ruthenium polypyridyl sensitizer, which will relax to the bipyrimidine-based ^{3}MLCT emissive state, from which the electron should have sufficient energy to photo-reduce molybdenum (the ^{3}MMCT state),

In order to determine whether the states are truly energetically ordered as depicted in *Figure 34*, the three components were examined separately. *Equation 9* below provides a way to approximate the change in free energy of electron transfer ΔG_{ET},[67] the driving force for the excited sensitizer, $[Ru(bpy)_2(bpym)]^*$, to reduce the catalytic metal center, $[MoO(bpym)_2]$:

$$\Delta G_{ET} = E_{ox} - E_{red} - E_T - e^2/(\varepsilon d) \qquad \textit{Equation 9.}$$

[65] Allen, G.H.; White, R.P.; Rillema, D.P.; Meyer, T.J. *J. Am. Chem. Soc.* **1984**, *106*, 2613.
[66] Nitadori, H.; Takahashi, T.; Inagaki, A.; Akita, M. *Inorg. Chem.* **2012**, *51*, 51.
[67] Rehm, D.; Weller, A. *Ber. Bunsen-Ges. Phys. Chem.* **1969**, *73*, 834-839.

where E_{ox} represents the $Ru^{III/II}$ oxidation potential, E_{red} represents the $Mo^{IV/III}$ and $Mo^{III/II}$ reduction potentials for the first and second photoreduction respectively, E_T is the energy available from the long-lived ^{3}MLCT $Ru^{III}(bpym^{-}\bullet)$ state, ε is the solvent's dielectric constant, and *d* is the distance between metal centers. In the case of an organic solvent, such as DMSO, the dielectric constant, ε_{DMSO} is sufficiently large that the last term in the equation above can be ignored. The equation compares the energy required to remove an electron from Ru^{II} and place it on Mo^{IV} and Mo^{III} to the energy available to the electron in the excited state. A negative ΔG_{ET} implies that electron transfer from the excited state to molybdenum is energetically favorable.

The values of E_{ox} and E_{red} were determined by cyclic voltammetry. The $[Ru^{II}(bpy)_2(bpym)]^{3+/2+}$ reduction potential was found to be 0.3 V vs. $Fc^{+/0}$ in DMSO. This is the value used for E_{ox}. From the cyclic voltammograms in the *Figure11* above in **Chapter 3**, the $Mo^{IV/III}$ and $Mo^{III/II}$ reduction potentials were found to be -1.45 and -1.75 V vs. $Fc^{+/0}$ respectively. These are the values used for E_{red} for the first and second photoreduction of the molybdenum core.

To investigate the ^{3}MLCT excited state, UV-vis absorption and emission spectra were measured for $[Ru(bpy)_2(bpym)]^{2+}$ in DMF, and are visible in *Figure 35* below. The absorption spectrum showed the bands typical of a ruthenium (II) polypyridyl complex. The high energy bands in the UV portion of the spectrum represented the π*←π transitions on the bipyridyl ligands, while the collection of lower energy bands in the visible (400 nm and 475 nm) represented the overlapping absorption envelopes for the (bpy)←Ru and (bpym)←Ru singlet metal to ligand charge transitions respectively. *Figure 35* shows the emission spectra taken at different excitation wavelengths, which

are indicated on the unlabeled axis. Although the emission was maximum, when the complex was excited with 480 nm light (corresponding to the (bpym)←Ru excitation), the complex emitted when it was excited with higher energy light as well.

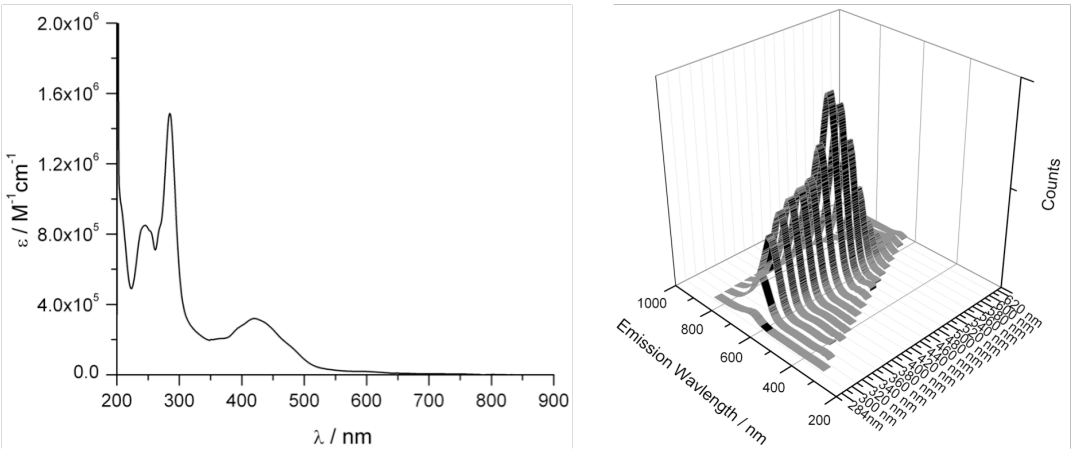

Figure 35. The UV-vis absorption spectrum of $[Ru(bpy)_2(bpym)]^{2+}$ was taken in DMF. The intense absorptions in the UV correspond to $\pi* \ \pi$ transitions localized on one bipyridyl ligand. The overlapping absorption envelopes in the visible represent ^{1}MLCT transitions from ruthenium to bpy and to bpym. The fluorescence spectra of $[Ru(bpy)_2(bpym)]^{2+}$ were also taken in DMF at room temperature.

Figure 36 below show all of the emission spectra plotted together, as well as the fluorescence intensity at the emission maximum (λ_{max}= 662 nm) as a function of excitation wavelength. It's evident from the emission spectra that regardless of the excitation wavelength the complex emitted solely from the ^{3}MLCT $Ru^{III}(bpym^{-}\bullet)$ state. All of the excitations resulted in emission at 662 nm with emission intensity from each state ordered as follows: π*←π << (bpy)←Ru < (bpym)←Ru. This was as expected, because the time required to relax to the $Ru^{III}(bpym^{-}\bullet)$ state resulted in loss of fluorescence quantum yield.

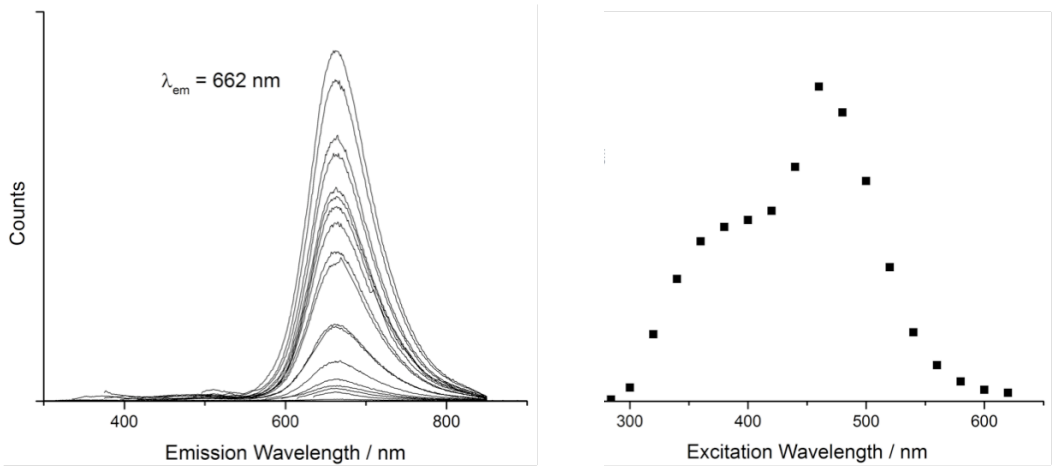

Figure 36. Regardless of excitation wavelength, $[Ru(bpy)_2(bpym)]^{2+}$ always emitted from the bpym-based ^{3}MLCT state, with λ_{max} = 662 nm (left). Emission was maximum when the complex was excited into the bpym-based ^{3}MLCT state (right).

$Ru^{III}(bpym^{-}\bullet)$ state. All of the excitations resulted in emission at 662 nm with emission intensity from each state ordered as follows: π*←π << (bpy)←Ru < (bpym)←Ru. This was as expected, because the time required to relax to the $Ru^{III}(bpym^{-}\bullet)$ state resulted in loss of fluorescence quantum yield.

The value for E_T, the amount of energy available to do redox chemistry from the $Ru^{III}(bpym^{-}\bullet)$ excited state, was found from the high-energy edge of the emission band in *Figure 36*. The highest energy emission signal was used, because it represented the return to the vibrational ground state of the electronic ground state, as opposed to a vibrationally excited state of the electronic ground state. The highest energy emission was the best indicator of the energy available in the ^{3}MLCT excited state. The high-energy edge of the emission spectra in *Figure 36* was approximately 580 nm, which corresponded to an energy of 2.1 eV.

Plugging these values into *Equation 9* above, ΔG_{ET} was calculated to be 0.3 – (–1.45) – (2.1) = –0.35 eV for the first photoreduction and 0.3 – (–1.75) – (2.1) = –0.05 eV

for the second photoreduction. This analysis indicates that *Figure 34* above accurately depicts the relative ordering of the excited state energies, and that electron transfer from the ^{3}MMCT state is energetically favorable. In order to increase the driving force for electron transfer, one could increase the energy of the bpym π* orbital, make the $Mo^{III/II}$ couple more positive, or perhaps most realistically, make the $Ru^{III/II}$ couple less positive by adding highly π-donating ligands in place of one of the π-acidic bipyridine ligands. In the actual molecular device, there will be other competing processes from the excited state that will significantly limit the efficiency with which the complex performs photochemistry.

Chapter 6: Conclusions and Outlook

The complex $[MoO(bpy)_2]^{2+}$ **(2)** served as an effective electrocatalyst for proton reduction from tosic acid in DMSO. **(2)** eliminated H_2 with a measured rate constant, k_{cat} = 1.24 Hz. The catalytic mechanism for hydrogen evolution at **(2)** is proposed to be 1) an initial one-electron, two-proton reduction at -1.50 V vs. $Fc^{+/0}$, 2) a second reduction at approximately -1.75 V vs. $Fc^{+/0}$ followed by 3) the elimination of H_2 from the complex possibly via a similar mechanism to the computationally proposed α–H abstraction from oxomolybdenum(IV) centers in similar complexes.[68]

The complex $[MoO(bdt)_2]^{2-}$ **(3)** was evaluated as an electrocatalyst for proton reduction, and the catalytic mechanism was investigated using a combination of spectroscopy, electrochemistry, and spectroelectrochemistry. Such mechanistic insight

[68] J. Li and K. Yoshizawa, *Angew. Chem. Int. Ed.*, 2011, **50**, 11972.

is necessary when designing electrocatalysts with the aim of improving catalyst properties such as overpotential and turnover frequency.

$[Ru(bpy)_2(bpym)]^{2+}$ was investigated as a light sensitizer for incorporation into a molecular photocatalytic device. The viability of the $Mo^{IV}O(bipyridyl)_2$ catalytic motif as an electrocatalyst for proton reduction has been established by studying **(2)**. The energetics of the proposed molecular device, $[(bpy)_2Ru(bpym)MoO(bpym)Ru(bpy)_2]^{6+}$ (see *Figure 33*) have been examined with a combination of electrochemistry and spectroscopy. It has been confirmed that the sensitizers offer sufficient energy to power hydrogen evolution at the molybdenum center in the proposed molecular photocatalyst.

Future work will focus on synthesizing the heterometallic, tri-nuclear molecular device, and then examining the device's electronic structure and efficacy as a photocatalyst.

Acknowledgements

Emily Nelson – Discovered and performed the synthesis of **(2)** and **(3)**, and performed the majority of the electrochemistry in chapters 3 and 4. She was an outstanding graduate student mentor, good chemistry discussion partner, and source of sage advice. She is also a lot of fun.

Professor Bartlett (Bart) – Bart is a great advisor, professor, and scientist. He introduced me to and sparked my interest in inorganic chemistry, for which I am very grateful. He is also a lot of fun.

The Bartlett Lab – I am glad that I chose this lab. Science in the Bartlett lab is interesting, relevant, and conducted at a high level. More importantly each individual lab member is an interesting, friendly individual, whom I am glad that I know.

University of Michigan, Department of Chemistry – Provided summer research fellowships in the summers of 2010 and 2011.

Beverly Lange – Bev is the glue that holds the chemistry department together. She has helped me immensely. She is also a lot of fun.

Appendix

Derivation of Expressions for k_{cat} and k_f *using Michaelis Menten kinetics* –

For the reaction $MoO + 2e^- + 2H^+ \underset{k_r}{\overset{k_f}{\leftrightarrow}} MoOH_2 \xrightarrow{k_{cat}} MoO + H_2$, assume that the concentrations of reactants and products change at the rates described by the expressions below:

$$\frac{d[H^+]}{dt} = -k_f[MoO][H^+]^2 + k_r[MoOH_2] \qquad (a)$$

$$\frac{d[MoO]}{dt} = -k_f[MoO][H^+]^2 + k_r[MoOH_2] + k_{cat}[MoOH_2] \qquad (b)$$

$$\frac{d[MoOH_2]}{dt} = +k_f[MoO][H^+]^2 - k_r[MoOH_2] - k_{cat}[MoOH_2] \qquad (c)$$

$$\frac{dn_{H_2}}{dt} = k_{cat}[MoOH_2] \qquad (d)$$

The rate represented in (d) is k_{obs}, the rate of hydrogen production. To overcome the fact that one cannot measure $[MoOH_2]$ during the experiment to obtain an expression for k_{obs}, it is necessary to assume that the concentration of $[MoOH_2]$ remains steady during the course of the experiment:

$$\frac{d[MoOH_2]}{dt} = 0$$

$$\Rightarrow k_f[MoO][H^+]^2 = k_r[MoOH_2] + k_{cat}[MoOH_2]$$

$$\Leftrightarrow \frac{(k_r + k_{cat})}{k_f} = \frac{[MoO][H^+]^2}{[MoOH_2]}$$

Now the conservation of catalyst (assumption 3 in **Chapter 3**) is used:

$$\frac{(k_r + k_{cat})}{k_f} = \frac{[MoO][H^+]^2}{[MoOH_2]} \quad and \quad [MoO]_0 = [MoO] + [MoOH_2]$$

$$\Rightarrow \frac{(k_r + k_{cat})}{k_f} = \frac{([MoO]_0 - [MoOH_2])[H^+]^2}{[MoOH_2]}$$

$$\Leftrightarrow [MoOH_2] = \frac{[MoO]_0[H^+]^2}{\frac{(k_r + k_{cat})}{k_f} + [H^+]^2} \quad and \quad k_r << k_f$$

$$\Rightarrow [MoOH_2] = \frac{k_f[H^+]^2}{k_{cat} + k_f[H^+]^2}[MoO]_0$$

Combining this expression for $[MoOH_2]$ with equation (d) above yields the final expression for the rate of hydrogen production and k_{obs}:

$$\frac{dn_{H_2}}{dt} = \frac{k_f k_{cat}[H^+]^2}{k_{cat} + k_f[H^+]^2}[MoO]_0$$

Substituting this expression for k_{obs} into the equation for catalytic current (*Equation 5*) yields:

$$i_c = nFA[cat]\sqrt{D\frac{k_f k_{cat}[H^+]^2}{k_{cat} + k_f[H^+]^2}}$$

which at low concentrations of acid simplifies to:

$$i_c = nFA[cat]\sqrt{Dk_f[H^+]^2} = nFA[cat]D^{1/2}k_f^{1/2}[H^+]$$

while at high concentrations of acid, it simplifies to:

$$i_c = nFA[cat]\sqrt{Dk_{cat}}$$

Kinetics Studies for $[MoO(bdt)_2](NEt_4)_2$ ***(3)*** *–*

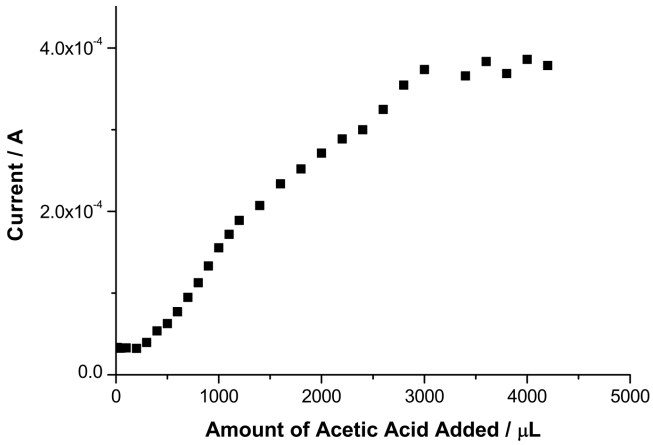

Figure S1. The catalytic wave maximum current for $[MoO(bdt)_2]$ **(3)** has a linear dependence with the concentration of acetic acid, indicating that the catalyzed reaction is second order in acid concentration, as expected. At higher acid concentrations, it is independent of acid, because the current is limited by the frequency with which the catalyst can turn over hydrogen. This experiment is analogous to the experiment represented by the left half of *Figure 13.*

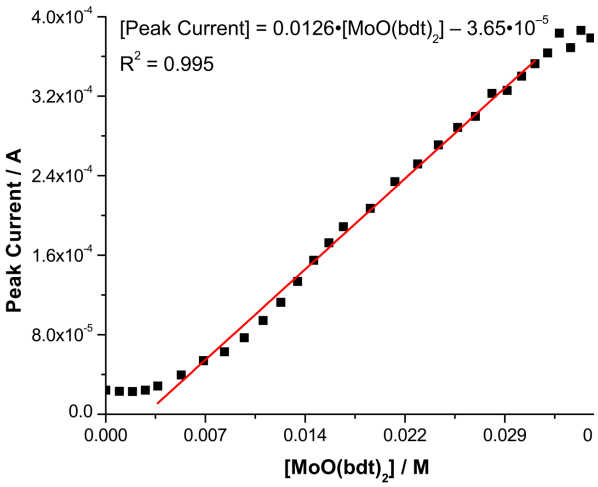

Figure S2. The catalytic wave maximum current for $[MoO(bdt)_2]$ **(3)** has a linear dependence with the concentration **(3)**, indicating that the catalyzed reaction is first order in **(3)**, as expected. This experiment is analogous to the experiment represented by the right half of *Figure 13.*